RMetS

ROYAL METEOROLOGICAL SOCIETY

The impact of vertical resolution on regional model simulation of the west African summer monsoon

Leonard M. Druyan,[a,b]* Matthew Fulakeza[a,b] and Patrick Lonergan[a,b]

[a] *Center for Climate Systems Research, Earth Institute at Columbia University, 2880 Broadway, New York NY 10025 USA*
[b] *The NASA/Goddard Institute for Space Studies, 2880 Broadway, New York NY 10025 USA*

ABSTRACT: The RM3 regional climate model is used to simulate the west African summer monsoon for six June–September seasons using NCEP reanalysis data for lateral boundary forcing. The study compares the performance of the previously published 16-level version with a newly tested 28-level version, both running on a horizontal grid with 0.5° spacing, in order to determine what improvements in simulations are achieved by increased vertical resolution. Comparisons between the performances include diagnostics of seasonal mean precipitation rates and circulation, vertical profiles of cumulus heating rates, frequencies of shallow and deep convection and diagnostics related to transient African easterly waves (AEWs). The characteristics of a composite AEW simulated at both vertical resolutions are presented. Results show that the most significant impact of increasing the vertical resolution is stronger circulation, stronger vertical wind shear and higher amplitude AEWs. The simulations with higher vertical resolution also achieve higher peaks of cumulus latent heating rates. Spatial–temporal correlations between simulated daily 700 mb meridional winds *versus* corresponding NCEP reanalysis data and simulated daily precipitation *versus* estimates from the Tropical Rainfall Measurement Mission (TRMM) archive were equally high at both vertical resolutions. Copyright © 2007 Royal Meteorological Society

KEY WORDS   west African monsoon; regional climate model; African easterly waves

Received 25 January 2007; Revised 4 September 2007; Accepted 8 September 2007

1. Introduction

This article analyses aspects of the simulated June–September west African monsoon (WAM) climate, with particular attention to the characteristics of African easterly wave disturbances (AEWs). Simulations are made with a regional/limited area model (LAM) on a 0.5° latitude by longitude grid, integrated at two vertical resolutions, at 16 and 28 vertical levels, respectively. The regional model is referred to as RM3 since it has undergone two major improvements (Druyan *et al.*, 2004; Druyan and Fulakeza, 2005) since its first application to WAM studies (Druyan *et al.*, 2000, 2001).

The impact of the increased vertical resolution is evaluated by comparing simulations to each other and to empirical evidence in order to better appreciate the relevance of results to the real world. Druyan *et al.* (2006) previously used lateral boundary conditions from NCEP reanalysis (hereafter NCPR) to drive RM3 summertime WAM simulations. Such dynamic downscaling of the reanalysis creates mesoscale resolution data sets (e.g. Leung *et al.*, 2004). The downscaling is not an interpolation of the forcing analysis because the RM3 integrates the governing equations on a finer grid and also benefits from a higher resolution distribution of terrain topography

and land surface (LS) characteristics. Accordingly, downscaled representations of the climate can be quite different from the driving analysis. Druyan *et al.* (2006) showed that NCPR-driven RM3 simulations produce time-space distributions of WAM precipitation that are highly correlated with Tropical Rainfall Measuring Mission (TRMM) daily estimates in continuous 4-month summer simulations with no perceptible deterioration trend. However, RM3 daily precipitation rates generally had a smaller range than corresponding TRMM data. The simulations achieved too few very high and very low rates.

The summer WAM climate features a northward meridional temperature gradient over west Africa that creates a westward-directed vertical wind shear (thermal wind). Accordingly, near-surface monsoon southwesterlies reverse direction with altitude, ultimately creating the mid-tropospheric African easterly jet (AEJ). The AEJ core is formed by a reversal of the meridional temperature gradient above 700 mb, which in turn is enhanced by latent heat release within the convective towers of the Intertropical convergence zone (ITCZ) and dry convection to the north (Thorncroft and Blackburn, 1999). Vertical wind shear below the AEJ is a source of energy for the growth of AEWs. In order to simulate realistic AEWs, models must achieve realistic representations of the thermal structure and the AEJ.

Mid-tropospheric transient AEWs have a role in modulating the precipitation of west Africa during the summer monsoon season (Reed *et al.*, 1977; Duvel, 1990;

* Correspondence to: Leonard M. Druyan, Center for Climate Systems Research, Earth Institute at Columbia University, 2880 Broadway, New York NY 10025 USA.
E-mail: LDruyan@giss.nasa.gov

Druyan *et al*., 1996; Lavaysse *et al*., 2006). Much of the Sahel's seasonal rainfall occurs in organized squall lines (Lamb and Peppler, 1991) and many of them are imbedded within AEWs (Fortune, 1980; Landsea and Gray, 1992), so these synoptic disturbances are quite relevant to the local climate variability (Ward *et al*., 2004). Refined understanding of AEW behaviour and characteristics will contribute to improved regional planning as well as to advancing the prospects of seasonal forecasting. Given the centrality of the AEJ and AEW in the evolution of the summertime climate over west Africa, models are challenged to produce realistic simulations, but high spatial resolution is a definite asset.

Diedhiou *et al*. (1999) investigated the properties of AEWs based on NCPR and European Center for Medium-range Weather Forecasts (ECMWF) daily reanalysis data. Significant differences were evident in results from the NCPR *versus* the ECMWF data sets. No attempt was made to relate perceived inter-annual trends in circulation to the inter-annual variability of WAM precipitation. Both the NCPR and ECMWF reanalyses used by Diedhiou *et al*. (1999) to construct their multi-year AEW climatology represent meteorological variables on 2.5 by 2.5° grids, based on model simulations that resolve gradients and terrain slopes on equivalent grid intervals of about 210 and 125 km, respectively. Even though represented at the same resolution, analysed wave properties differed between the two systems, probably because of model dependence.

Druyan *et al*. (2006) discussed the results of six June–September RM3 simulations over west Africa, which used NCPR for lateral boundary conditions. The horizontal grid for the simulations had 0.5° spacing and the primitive equations were integrated at 16 vertical sigma levels. Spectra of RM3 700 mb meridional wind (*v7*) time series showed peaks for 3–6 day periods over swaths of the model domain related to the westward propagation of AEWs, in particular along 17 and 4 °N. Many AEWs were associated with significant rainfall. In fact, precipitation time series exhibited similar periodicities as *v7*, with spectral peaks at 4–5 day periods. The timing of mid-tropospheric waves in these RM3 simulations was highly correlated with their timing in NCPR. However, RM3 *v7* fluctuations had a consistently smaller range than corresponding NCPR or ECMWF *v7* time series, indicating that RM3 AEWs had lower amplitudes. Negative impacts of this deficiency on other simulated variables were not investigated, but subsequent tests suggested that increased vertical resolution could have a positive effect on wave amplitudes.

The current study was motivated by the hypothesis that higher vertical resolution would improve the RM3 simulation of AEW amplitudes and associated precipitation rates, thereby also improving the simulation of the seasonal WAM and its variability. The advantages of increased vertical resolution for WAM simulations have not been previously discussed in the literature.

GCM (Hadley Centre Atmosphere General Circulation Model–HadCM3) experiments by Inness *et al*. (2001)

showed that increasing model vertical resolution created differences in the variability of simulated tropical upper tropospheric zonal winds associated with the Madden-Julian Oscillation (MJO). In simulations made at the lower vertical resolution of 19 levels, minimal variability was realized. Increasing the vertical resolution to 30 levels achieved an increase in the amplitude of zonal wind fluctuations associated with the MJO sufficient to match observational evidence. Inness *et al*. (2001) speculated that the improvement resulted from stronger upper tropospheric westerlies in the 30-level version, which in turn promote more efficient wave propagation from the extra-tropics. A stronger simulated AEJ would similarly have an important impact on AEWs. The present study examines the results of repeating the Druyan *et al*. (2006) RM3 simulations with increased vertical resolution. The article analyses the impact of increasing the number of model sigma levels from 16 to 28 on the representation of the summer WAM, and especially on the AEJ and AEWs.

2. Model and experiments

The study compares results from the 16-level version (hereafter RM3.16L or just 16L) with simulations made using the identical model, except with 28 vertical sigma levels (hereafter RM3.28L or just 28L). Table I shows the sigma levels at which geopotential height is computed and their nominal pressures for each version, showing that the resolution between 1000–100 mb was increased from 11 to 20 levels. Druyan *et al*. (2006) described the important components of the newest third-generation version, RM3, so only a brief description is given here. The RM3 uses the same LS process model used in the GISS GCM (Rosenzweig and Abramopoulos, 1997; Hansen *et al*., 2002). The LS model consists of two integrated parts, the soil and the canopy, and it conserves water and heat while simulating their vertical fluxes. The RM3 modelled soil is divided into six layers to a depth of 3.5 m, and the model distinguishes between five textures of soil. The canopy, modelled as a separate layer located above the soil, is responsible for the interception of precipitation, evaporation of accumulated water and removal of soil water through transpiration.

The Del Genio and Yao (1993) moist convection parameterization and the Del Genio *et al*. (1996) scheme for the effects of cloud liquid water have also been incorporated into the RM3. These are components originally developed for the GISS GCM, which has already been extensively applied to climate sensitivity studies (e.g. Hansen *et al*., 2002). The cloud liquid water scheme allows for life cycle effects in stratiform clouds and permits cloud optical properties to be determined interactively.

Fritsch and Carbone (2004) noted serious deficiencies in the current technology of modelling moist convection that is used as the basis for warm-season quantitative precipitation forecasting. Nevertheless, the RM3

Table I. Vertical model levels of $\sigma = p/p_s$. Nominal pressures of sigma levels are shown for $p_s = 1000$ mb.

RM3.16L		RM3.28L	
Sigma	Pressure (mb)	Sigma	Pressure (mb)
0.020	20	0.010	10
0.030	30	0.020	20
0.050	50	0.050	50
0.070	70	0.060	60
0.125	125	0.070	70
0.225	225	0.080	80
0.325	325	0.101	101
0.425	425	0.151	151
0.525	525	0.201	201
0.625	625	0.251	251
0.700	700	0.302	302
0.775	775	0.352	352
0.850	850	0.402	402
0.925	925	0.452	452
0.975	975	0.503	503
1.0	1000	0.553	553
		0.603	603
		0.653	653
		0.704	704
		0.754	754
		0.804	804
		0.854	854
		0.879	879
		0.905	905
		0.930	930
		0.955	955
		0.980	980
		1.0	1000

simulates time-space patterns of westward-propagating precipitation swaths that compare quite favourably with daily estimates from TRMM satellite data after an initial spin-up of about 6 days (Druyan and Fulakeza, 2005).

In the experiments described here, lateral boundary conditions (LBCs) are obtained from NCPR data four times daily. These externally specified field values are then merged with forecasted variables produced by the RM3 by weighting them with progressively decreasing weights inward within a buffer zone that completely surrounds the domain of interest, 35 °N–20 °S, 35 °W–35 °E (see, for example, Figure 2, below). Additional details for merging LBCs are described by Druyan *et al.* (2001).

This study examines six 4-month simulations, June–September (JJAS), 1998–2003, all initialized with NCPR atmospheric conditions, soil moisture and sea-surface temperatures on 15 May. These are years for which validating TRMM precipitation estimates were available for the original Druyan *et al.* (2006) study. Here, an additional data set for precipitation validation is referenced. National Oceanic and Atmospheric Administration/Climate Prediction Center (NOAA/CPC) for the

Famine Early Warning System (FEWS), version 2, provides relevant gridded estimates of precipitation rates for June–September 2001–2003, based on combining rain gauge and METEOSAT remote radiometric measurements (hereafter CPC/FEWS). Herman *et al.* (1997) explained the methodology, but version 2 was only implemented in 2000.

Section 3 discusses the results of the study, addressing, in order, the mean circulation, circulation variability, the mean precipitation, precipitation variability, the structure of a composite AEW and cumulus convection characteristics.

3. Results

3.1. Mean circulation features

Figure 1(a) shows a latitude-pressure cross-section of the RM3.28L zonal wind along 0° longitude, for JJAS 1998–2003. Figure 1(b) shows the corresponding field for the RM3.16L and Figure 1(c) for NCPR. Results for 28L differ from 16L and NCPR mainly regarding the core speed of the AEJ, while they agree that this core is at 600 mb. With the much stronger vertical wind shear of the 28L, its core easterlies are about 4 m s^{-1} stronger. Positive vertical shear above the jet core is also stronger for 28L. Near-surface zonal winds for 28L show good agreement with NCPR. Compared to the 28L results, the 16L mid-tropospheric zonal winds better resemble NCPR, but the 16L monsoon westerlies and Harmattan easterlies at 925 mb are about 1 m s^{-1} weaker than indicated by NCPR. Figure 2 shows that within the diagonal that marks the 700 mb extension of the AEJ over west Africa, the 28L zonal wind jet core is about 10% more extreme than NCPR. Since 28L easterlies are also stronger over the equatorial Atlantic and the Gulf of Guinea, gradients south of the AEJ (over Gulf of Guinea coastal states) are weaker than for NCPR. The AEJ core is about 2 m s^{-1} weaker in the 16L simulation, which is even weaker than in NCPR. The gradient south of the 16L AEJ is also weaker than for the 28L.

A zone of maximum vorticity variance is created along a trajectory of transient cyclonic disturbances. Accordingly, Reed *et al.* (1988) deduced AEW trajectories based on gridded data from ECMWF analysis and forecasts projected on a 3° by 3° latitude–longitude grid by mapping the 700 mb vorticity variance filtered for 2.9–4.0 and 2.9–4.7 day periods. Their analysis was confined to August–September 1985 and their Figure 4 showed a northerly AEW track along 21 °N as well as a more southerly one between 12–15 °N. Subsequently, Thorncroft and Hodges (2001) tracked AEW vorticity maxima at 600 and 850 mb over west Africa and the Atlantic Ocean during the 20-year period 1979–1998. They used ECMWF analyses created by assimilating observations at a similar horizontal resolution (T42 or about 2.8°), showing the most frequent trajectories crossing west Africa along approximately 10 °N. Druyan *et al.* (2006)
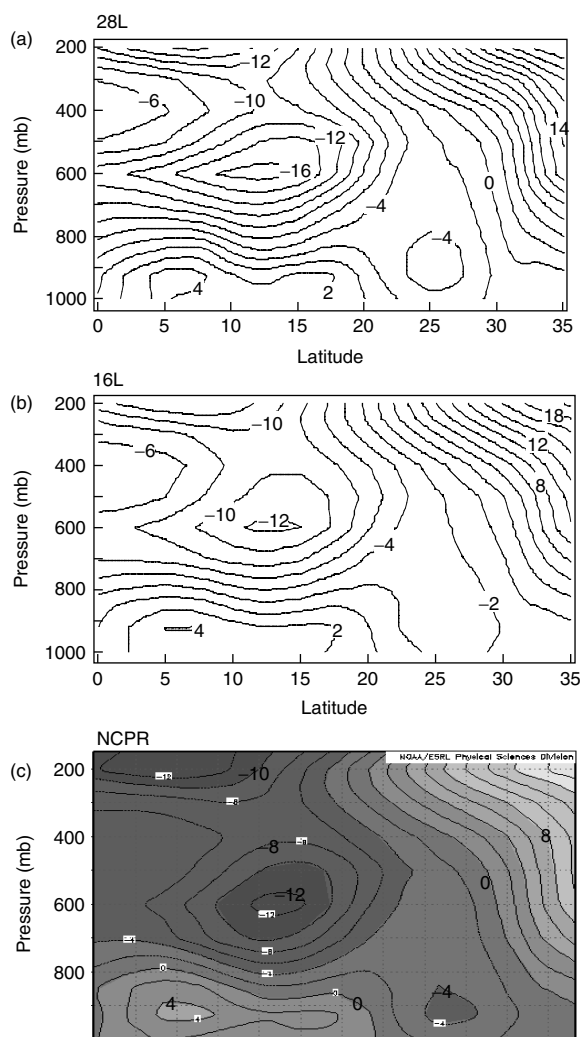
Figure 1. Cross-sections of zonal winds (m s^{-1}) along 0° longitude, for June–September 1998–2003. (a) RM3.28L, (b) RM3.16L and (c) NCPR (courtesy NOAA/CDC).

Figure 2. Horizontal distributions of zonal winds (m s^{-1}) at 700 mb, for June–September 1998–2003. (a) RM3.28L, (b) RM3.16L and (c) NCPR (courtesy NOAA/CDC).

showed spatial distributions of variances of 700 mb vorticity time series (four times per day) from 1 August to 30 September (AS), filtered for 3–6 day periods from each season simulated by the 16-level RM3. The distribution for AS 1998 indicated one AEW trajectory along 21 °N, and a second near 13 °N, similar to the Reed *et al.* (1988) results for 1985. In fact, the patterns for 5 of the 6 years (except AS 2000) also implied dual tracks. During AS 1999, the southernmost maxima implied a diagonal AEW path crossing from 6–13 °N, similar to the Thorncroft and Hodges (2001) results that consider vorticity maxima. The AS 2000 and AS 2002 data implied very distinct tracks closely following 11 and 15 °N, respectively. Vorticity variance amplitudes were particularly strong for AS 2001 over Atlantic coastal waters.

Figure 3(a) and (b) shows the spatial distributions of vorticity variance, from JJAS 2003 700 mb vorticity time series simulated by RM3.28L and RM3.16L, and filtered to include only 3–6 day periodicities. Results from both models indicate AEW tracks along 16 and 9 °N. The
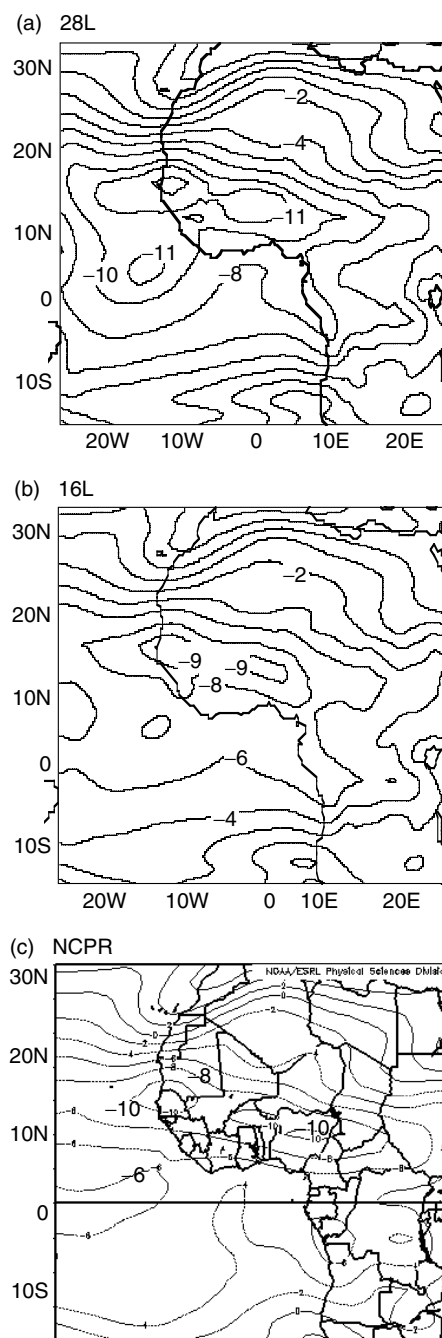
RM3.28L vorticity variances are about 65% stronger than the RM3.16L vorticity variances. In fact, the higher amplitudes detect AEW tracks in 28L that begin further east, near 0° longitude. Maximum vorticity variances in both cases imply a strengthening of the cyclonic systems as they move out over Atlantic coastal waters. Since the vorticity tracks change from season to season, the six-season composite is not very informative. In order to appreciate the inter-annual variability, Figure 3(c) and (d) shows north–south transects of the simulated 700 mb vorticity variance along 15 °W for each of the six seasons. Peaks occur at the latitudes where AEW tracks intersect
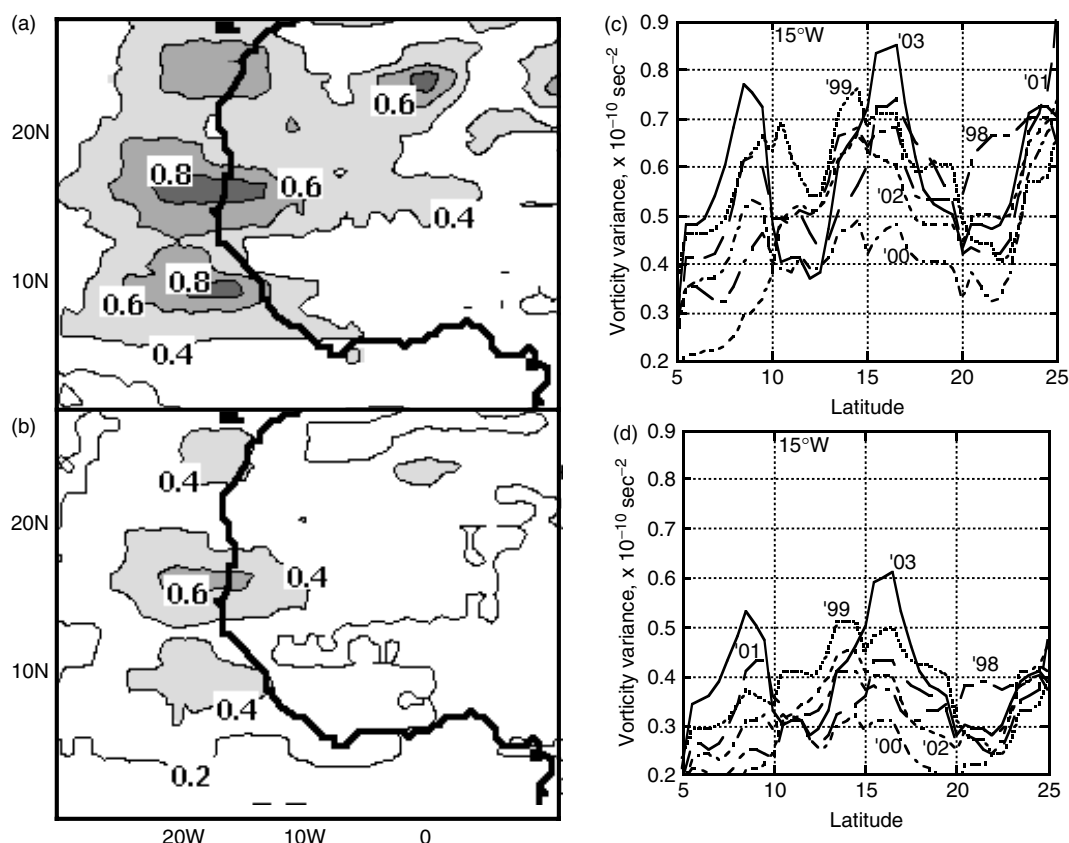
Figure 3. Variance of JJAS 700 mb vorticity time series ($\times 10^{-10}$ s^{-2}) (4$\times$ per day) filtered to include 3–6 day periods (a) RM3.28L horizontal distribution for JJAS 2003, (b) RM3.16L horizontal distribution for JJAS 2003, (c) and (d) North to south transects for each JJAS along 15 °W, for 28L and 16L simulations, respectively.

15 °W. In addition to the aforementioned tracks along 16 and 9 °N, peaks indicate AEW traversals during other years at 14 and 11 °N. JJAS 2000, on the other hand, is not distinguished by strong vorticity variance, indicating either fewer or weaker AEWs during that season. The corresponding transects for 16L (Figure 3(d)) show implied AEW tracks that parallel the 28L results, but all of the 28L magnitudes are at least 50% higher.

3.2. Circulation variability

Observations show that AEWs often feature closed cyclonic circulations in the lowest atmospheric layers, which are associated with open wave structures near 700 mb. AEWs that traverse west Africa cause periodic wind fluctuations, most prominently in the meridional component of the circulation. Amplitudes of these fluctuations are strongest in the mid-troposphere, usually at about 700 mb, south of the AEJ, although according to Pytharoulis and Thorncroft (1999), at lower altitudes farther north.

Figure 4 shows Hovmöller time-longitude plots of 700 mb meridional wind components (*v7*), averaged over 5–15 °N, for July–August 2002. *V7* has been plotted once daily (at 12 UT) for RM3 at each of the two vertical resolutions and these distributions are compared to corresponding NCRP and ECMWF 40-year reanalysis (ERA-40) July–August (JA) 2002 data. Patterns of westward-propagating centres of alternating southerly and northerly

circulation are prominent in each analysis, and the timing of these bands for each data set is closely synchronized with the others. The *v7* extremes are generally several m s^{-1} higher in August than in July. The slopes of the alternating positive and negative bands imply AEW westward speeds of 5°–10° per day (5.8–11.6 m s^{-1}), and longitudinal distances between adjacent maxima or minima imply wavelengths of about 25° (approximately 2500 km) and 3–5-day periods. Reed *et al.* (1988) also deduced 2500 km AEW wavelengths from ECMWF data gridded with 3° spacing, but the finer RM3 computational grid allows more precise estimates. These speeds, periods and wavelengths are representative of estimates from previous empirical studies (Burpee, 1972; Reed *et al.*, 1977; Druyan *et al.*, 1996). Note the occasional differences in the timing/location of *v7* extremes between the NCRP and ERA-40 representations, even though they are both partially based on observations. Despite the great congruities in the timing of *v7* extremes, RM3.16L *v7* clearly show a smaller range of (positive and negative) values than *v7* of RM3.28L, NCPR and ERA-40. Similar Hovmöller time–longitude distributions of the daily 12 UT *v7*, averaged over 5–15 °N, were constructed for all months of July and August, except that ERA-40 data was not available for 2003. Comparisons for the other years were consistent with this evaluation for JA 2002, as can also be seen in Table II. The Table II gives the correlation coefficient between corresponding *v7* values from
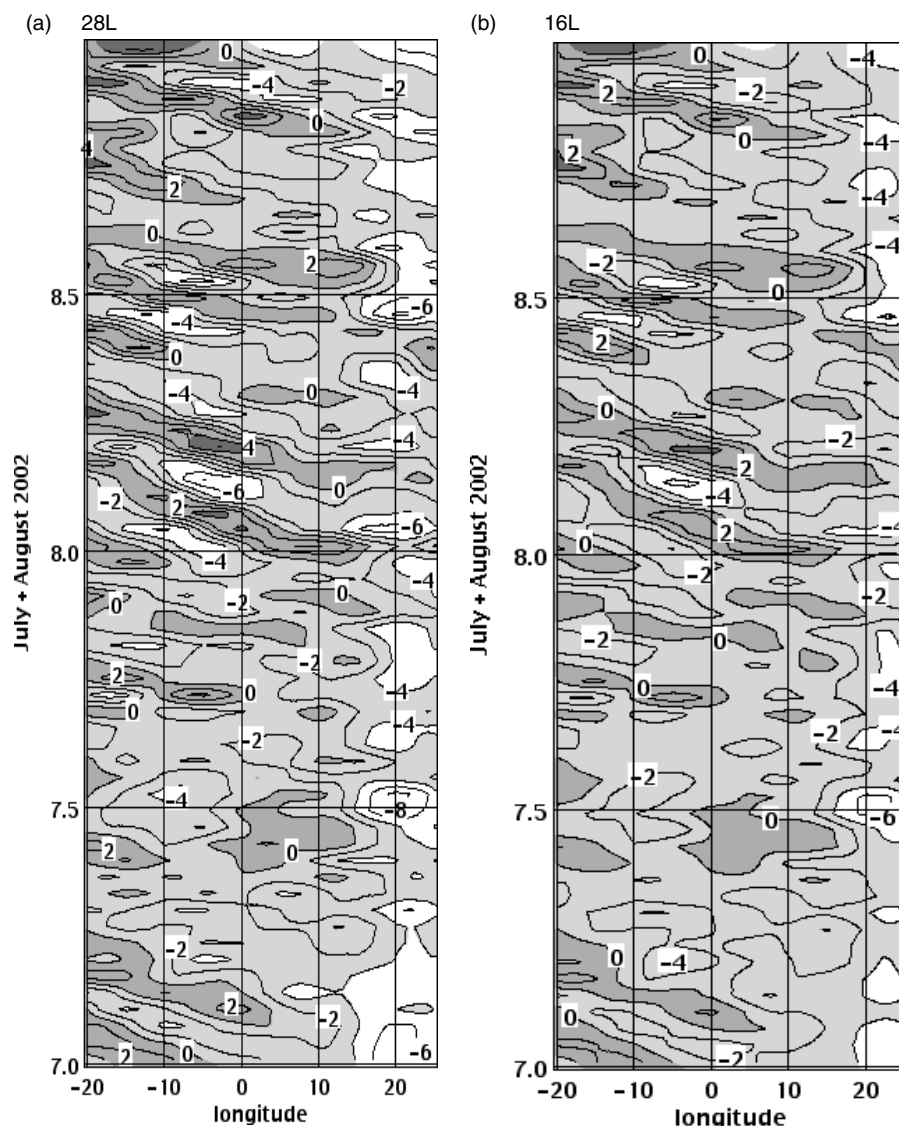
Figure 4. Hovmöller time-longitude distributions of 700 mb meridional wind (*v7*) daily at 12 UT, averaged over 5–15 °N, during July–August 2002. (a) RM3.28L simulation, (b) RM3.16L simulation, (c) NCPR (courtesy NOAA/CDC), (d) ERA-40 (courtesy ECMWF).

each time–longitude distribution and standard deviations of *v7* from each of the two model versions, NCPR and ERA-40. For this comparison NCPR and ERA-40 data were interpolated to the 0.5° grid. Note that increasing the vertical resolution of the RM3 increases the standard deviation of *v7* on the average from 75% of the NCPR value to about 93%. On the other hand, the vertical resolution seems not to affect the correlations with either NCPR or ERA-40.

Table II indicates that the RM3 Hovmöller time-longitude distributions of daily *v7* are consistently correlated (six-season average, $r = 0.98$) with the corresponding NCPR *v7*. The correlations are noteworthy because no NCPR *v7* data are provided to the simulations within the area covered by these distributions. Table II shows, however, that NCPR *v7* are imperfectly correlated with ERA-40 *v7*. Accordingly, correlations of model *v7* with corresponding ERA-40 *v7* are lower than against NCPR *v7* (although statistically significant) and they reflect the disparities between the two reanalysis data sets. These

results show the sensitivity of the regional model result to the driving data.

Do NCPR data that form the LBC along the eastern boundary of the domain already contain AEWs? The periodicity of successive AEWs can be monitored by Fast Fourier Transform (FFT) analysis of *v7* time series for entire seasons. Figure 5(a) shows the spectra of NCPR *v7* JJAS 2003 time series at 15 °N, 35 °E. This distribution has a very narrow spectral peak for 5-day periodicity that barely exceeds the threshold for 95% statistical significance. The peak perhaps represents incipient AEWs, but spectral amplitudes within the remainder of the period range associated with AEWs (roughly 3–6 days) are low. By way of contrast, the spectra of the 28L JJAS 2003 *v7* simulation at 15 °N, 10 °W (Figure 5(b)) includes considerably higher amplitudes for periods between 3.5–4.5 days that are above the 95% significance threshold. Figure 6 shows diagnostics related to AEW activity based on model simulated *v7* and 700 mb vorticity time series along an east-west transect near
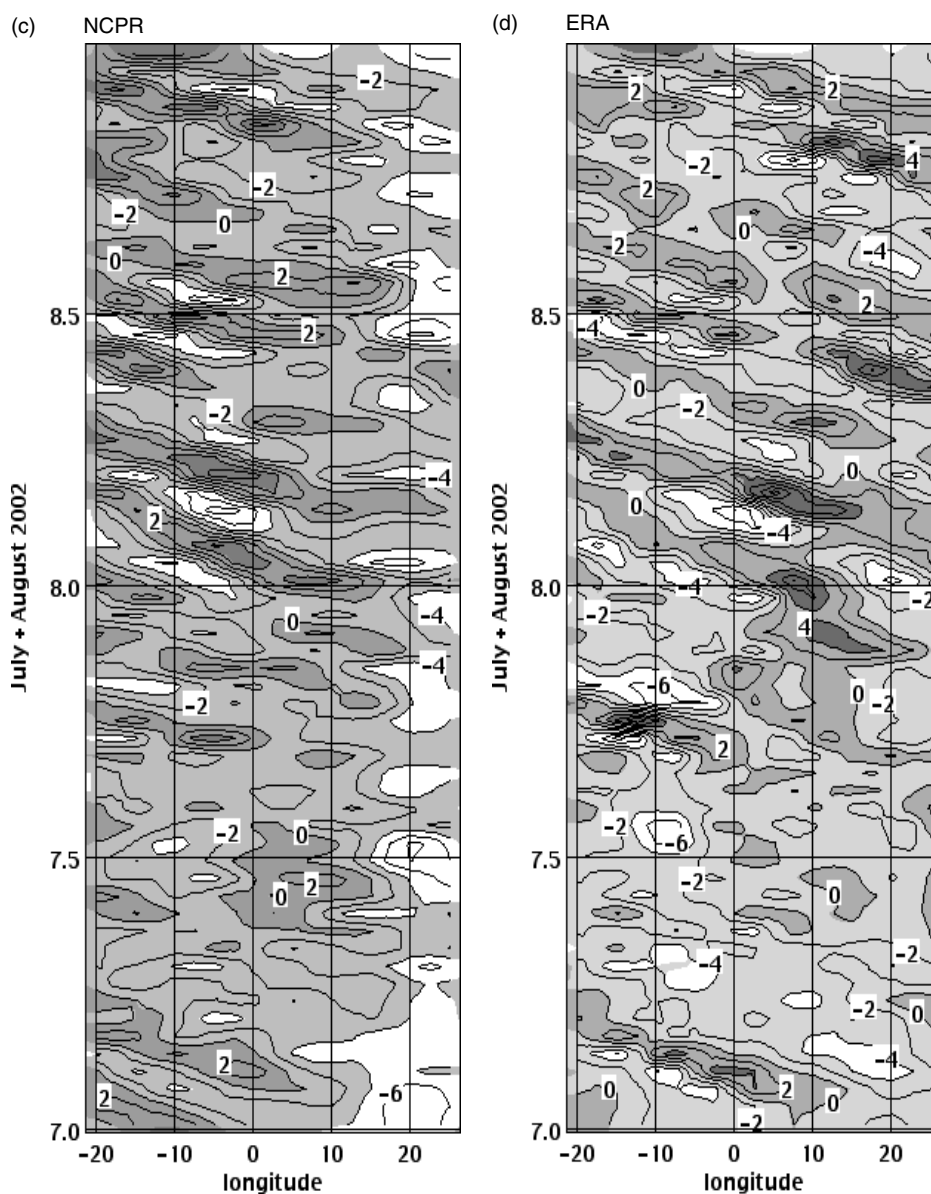
Figure 4. (*Continued*).

Table II. Standard deviations and correlation coefficients between Hovmöller time–longitude distributions of *v7* during July–August, as in Figure 4, but for JA 1998–2003. *5-year means, since ERA-40 data not available for 2003.

Statistic season	cc, 28L *vs.* NCPR	cc, 16L *vs.* NCPR	cc, 28L *vs.* ERA	cc, 16L *vs.* ERA	cc, NCPR *vs.* ERA	σ 28L m s⁻¹	σ 16L m s⁻¹	σ NCPR m s⁻¹	σ ERA m s⁻¹
1998	0.98	0.98	0.53	0.54	0.53	2.7	2.2	3.0	2.5
1999	0.98	0.98	0.61	0.63	0.61	2.6	2.1	2.9	2.6
2000	0.98	0.97	0.69	0.68	0.69	2.4	2.0	2.8	2.3
2001	0.97	0.99	0.73	0.72	0.72	2.5	2.0	2.0	2.4
2002	0.99	0.98	0.56	0.56	0.57	2.5	2.0	2.8	2.7
2003	0.98	0.98	–	–	–	2.7	2.1	3.0	–
6 year	0.98	0.98	*0.62	*0.63	*0.62	2.6	2.1	2.8	*2.5

15 °N. Vorticity variance and spectral amplitudes averaged for 3–6 day periods dramatically increase from east to west, approximately doubling in value between 30 °E and the African coast (17 °W). This demonstrates that

AEWs develop and strengthen within the RM3 domain. Moreover, NCPR lateral boundary values of these two diagnostics along 35 °E are similarly low. One can deduce that the meteorological data used for LBC (represented
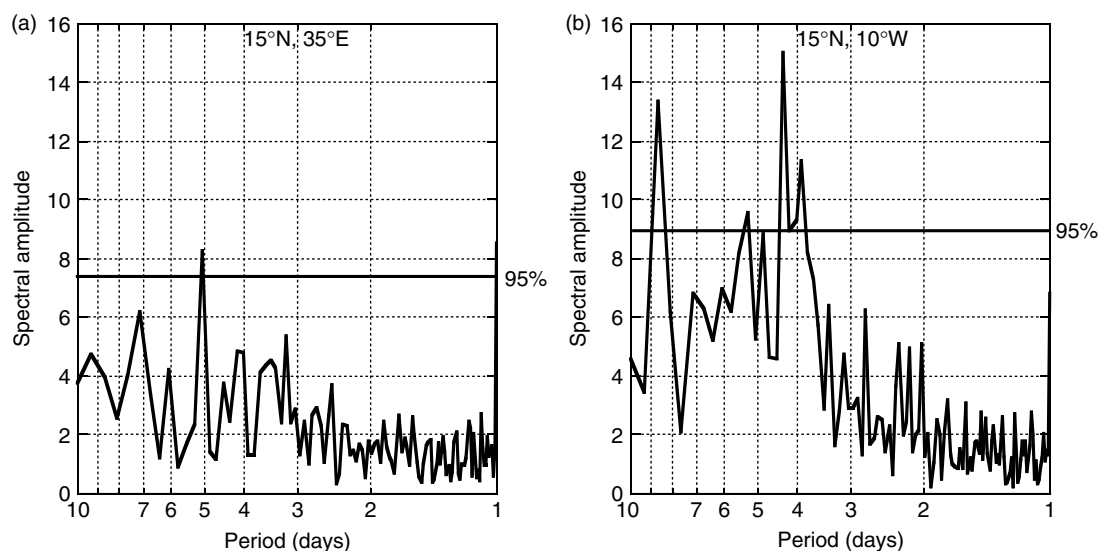
Figure 5. Spectra of JJAS 2003 time series (four times per day): (a) NCPR *v7* at 15 °N, 35 °E, (b) RM3.28L *v7* at 15 °N, 10 °W. The threshold for 95% statistical significance is indicated.

here by NCPR) provide the 'raw ingredients' by which AEWs are generated, developed and propagated. The influences of topography and energy fluxes from land surfaces are also undoubtedly important. The high correlation between the respective Hovmöller time-longitude distributions of daily *v7* indicates that the integrated RM3 treatment of AEWs parallels that of the NCPR model in their respective simulations in that the two models produce waves with the same timing. In addition, any observational input to the NCPR apparently sustains the RM3 interpretation. The limited correlations between *v7* of ERA-40 *versus* NCPR and ERA-40 *versus* RM3 are a consequence of differences between the ERA-40 analysis model *versus* NCPR and the RM3, possible differences in observational data assimilated by ERA-40 and NCPR and the contrasting evolutions of *v7* along 35 °E.
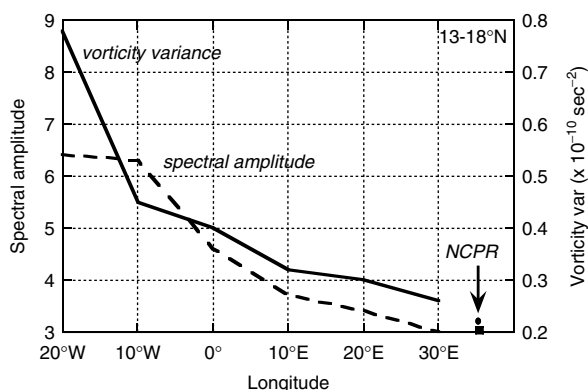
Figure 6. Longitudinal variations of two AEW diagnostics averaged over 13–18 °N. Spectral amplitudes are for 3–6 day periods from RM3.28L *v7* JJAS 2003 time series. Vorticity variances are for corresponding 700 mb vorticity time series filtered to include 3–6 day periodicities. NCPR values (dot is spectral amplitude, square is vorticity variance) are computed from NCPR data interpolated to the 0.5° grid. Based on time series with four times per day sampling.

Figure 7 compares RM3.16L and RM3.28L FFT spectra for *v7* JJAS 2003 time series at two grid elements. Spectral signatures at each location are almost identical for the two simulations, but 28L amplitudes are higher. At 15 °N, 10 °W both versions show a prominent peak for the 4.3 day period, and at 5 °N, 17 °W for the 3.7 day period. In both cases the 28L spectral peak is about 18% higher than the 16L spectral peak. This is consistent with higher 28L *v7* oscillations discussed above. The considerable energy for *v7* fluctuations within the interval of 3.5–5 day periods is consistent with earlier results (Burpee, 1972; Reed *et al.*, 1977; Druyan *et al.*, 1996). In addition, at 15 °N, 10 °W there is a prominent and statistically significant spectral peak for the 8.6 day period for both *v7* series, showing evidence that the RM3 simulations are generating 6–9 day period waves that Diedhiou *et al.* (1999) documented in reanalysis data. Figure 8 compares the inter-annual variability of *v7* spectral amplitudes at 15 °N, 10 °W for both versions of the RM3. Spectral amplitudes are consistently highest in the range of 3.5–6 day periods, but 5.5 day period spectral amplitudes for JJAS 2000 were 15–35% weaker than for other seasons, implying less AEW activity. Figure 3(c) and (d) showed that vorticity variance along 15 °W was also quite low during JJAS 2000. The 28L spectra have higher amplitudes than the 16L spectra for all periods and all summer seasons.

Spatial patterns of spectral amplitudes averaged over 3–6 day periods for JJAS 2003 shown in Figure 9 are somewhat different from the vorticity variance distributions shown above in Figure 3, although the maxima also imply AEW tracks over 9 and 16 °N. Comparison of Figure 9(b) to Figure 9(a) shows that 28L spectral amplitudes for 3–6 day periods are about 20% stronger than 16L results. For the other seasons results sustained the finding that increased model vertical resolution increases spectral amplitudes, but does not change the spatial pattern. Note, however, that implied AEW
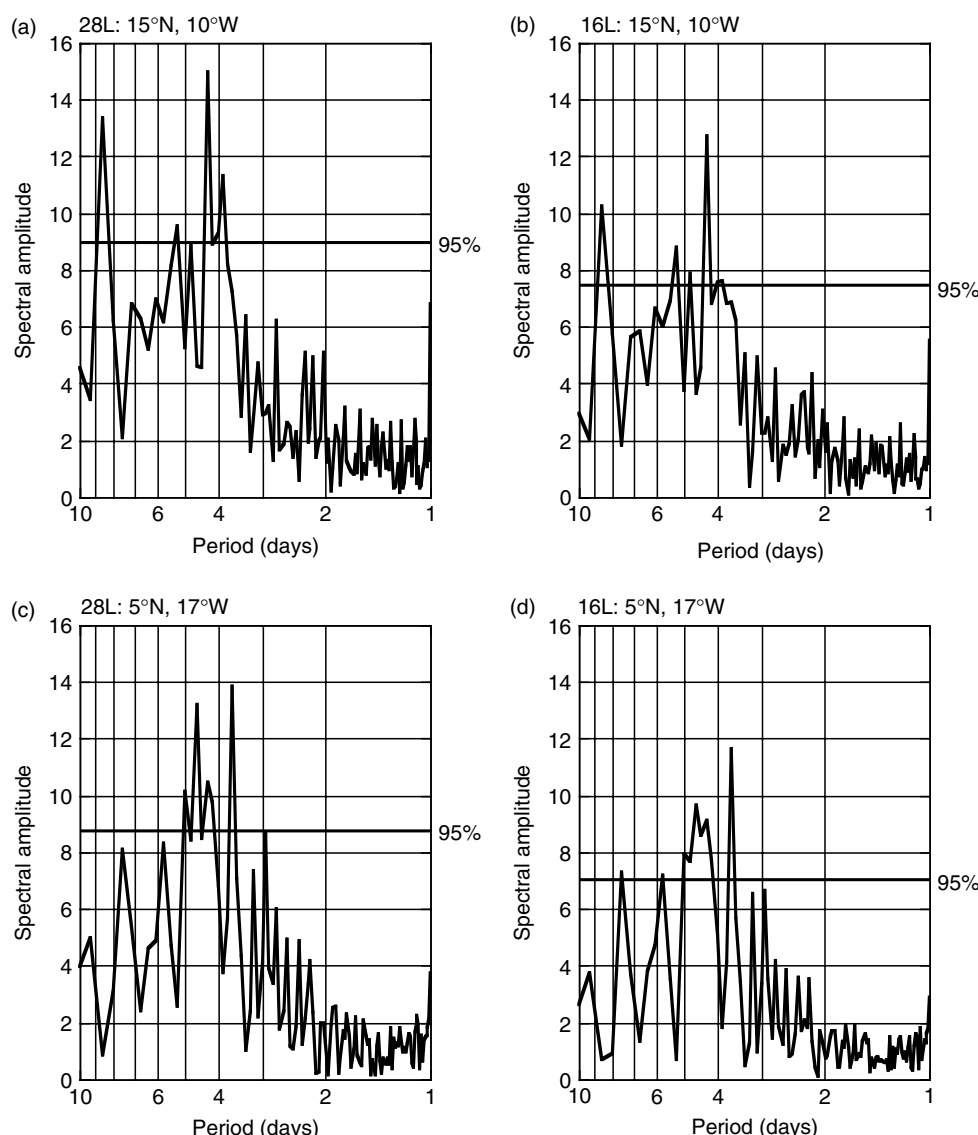
Figure 7. Spectra of JJAS 2003 *v7* time series (four times per day) at two grid locations for RM3.28L (a) and (c) and RM3.16L (b) and (d) simulations.

tracks over west Africa were varied from season to season.

3.3. Mean precipitation

High space-time correlations between RM3.16L daily precipitation and TRMM data were shown in Druyan *et al.* (2006). That study also reported a correlation of 0.73 between RM3.16L simulated time series of daily precipitation near Niamey *versus* daily observations from 34 rain gauges during July–September 2000. Figure 10 compares the spatial distribution of RM3 mean JJAS 1998–2003 precipitation for each of the two model versions to TRMM observations. The axis of maximum rainfall is observed to be along 10 °N and this is matched by both versions of the model. The 28L produces appropriately higher rainfall rates within the Atlantic ITCZ and along the southwest coast, but its ITCZ over west Africa is too wide and too rainy. The 16L underestimates Atlantic ITCZ and southwest coast

maxima, but is more consistent with TRMM further east. Both versions do not have a high enough maximum at the Cameroon coast. The spatial correlation between the 28L and TRMM fields in Figure 10 is 0.92, but between 16L and TRMM a lower 0.88. Figure 10(d) shows the differences between TRMM and CPC/FEWS JJAS 2001–2003 rainfall estimates. TRMM estimates of orographic precipitation along the southwest (Guinea) and Cameroon highlands are 2–6 mm d^{-1} greater than corresponding FEWS estimates. Druyan *et al.* (2006) showed that JJAS 1998–2000 precipitation rate estimates from rain gauge data (New *et al.*, 2002) were up to 6 mm d^{-1} *higher* than TRMM over these same areas, so one cannot easily deduce the actual biases of any particular data or the simulations. Discrepancies between the various data sets do emphasize the uncertainties of precipitation validation over west Africa. Figure 10(d) also indicates that TRMM estimates were *lower* than CPC/FEWS over the Atlantic ITCZ adjacent to Africa.
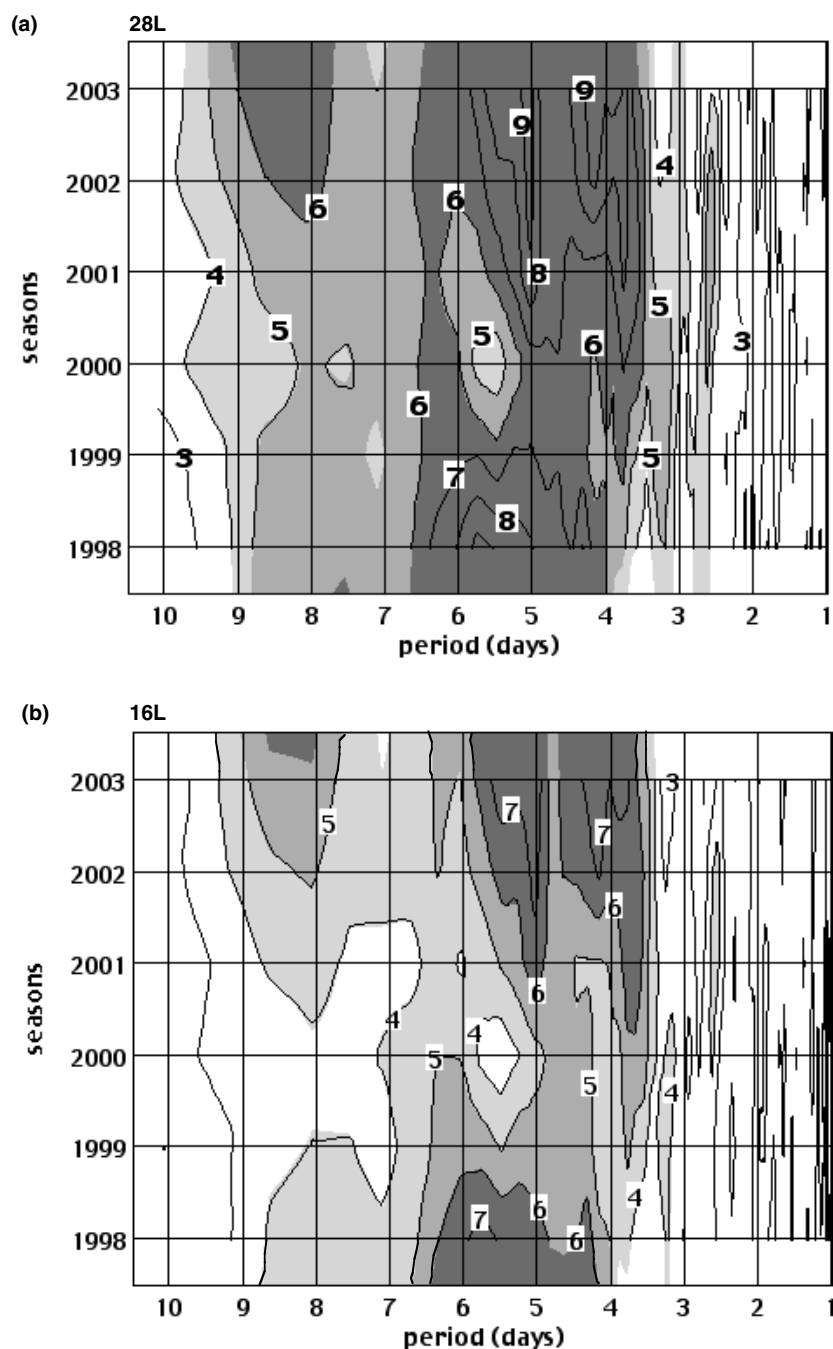
Figure 8. Inter-annual variability of spectral amplitudes, season *versus* period, for JJAS *v7* time series (four times per day) at 15 °N, 10 °W for (a) RM3.28L and (b) RM3.16L.

3.4. Precipitation variability

3.4.1. Time-latitude Hovmöller of precipitation

During the summer monsoon, RM3 and TRMM data show that the ITCZ precipitation maximum advances northward over west Africa until August and then retreats southward (Figure 11). Both model versions capture this meridional migration quite well, although the TRMM distribution is noisier, showing more isolated maxima and minima than the model. In fact, the six-season mean distributions in Figure 11(a) and (b) better resemble the time-space variability of TRMM data archived for 1° elements (not shown). The 16L moves the precipitation

maximum too far north during late June. Both versions simulate the northward jump in the heaviest precipitation from 6 to 10 °N between 1–6 July. Both also produce a number of precipitation maxima and several interruptions of the heavy precipitation that match TRMM observations in both latitude and time. The northern edge of the RM3 precipitation band does not extend far enough northward during parts of August and September. As an additional check on validation data, the CPC/FEWS time-latitude distribution of daily precipitation for JJAS 2001–2003 is compared to the corresponding TRMM Hovmöller chart in Figure 12. There is good agreement between these data sources for the heavy precipitation of early June,
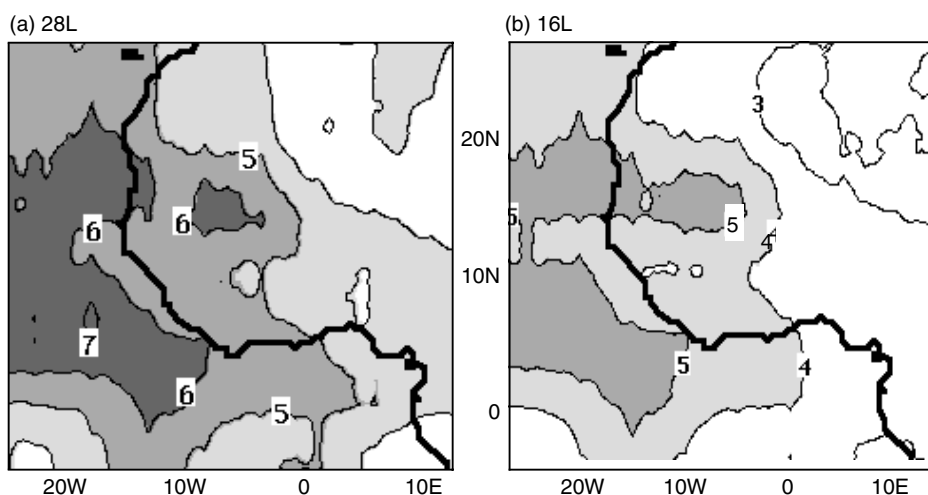
Figure 9. Spatial distributions of spectral amplitudes averaged over the 3–6 day period interval for *v7* JJAS 2003 time series (four times per day) simulated by (a) RM3.28L and (b) RM3.16L.
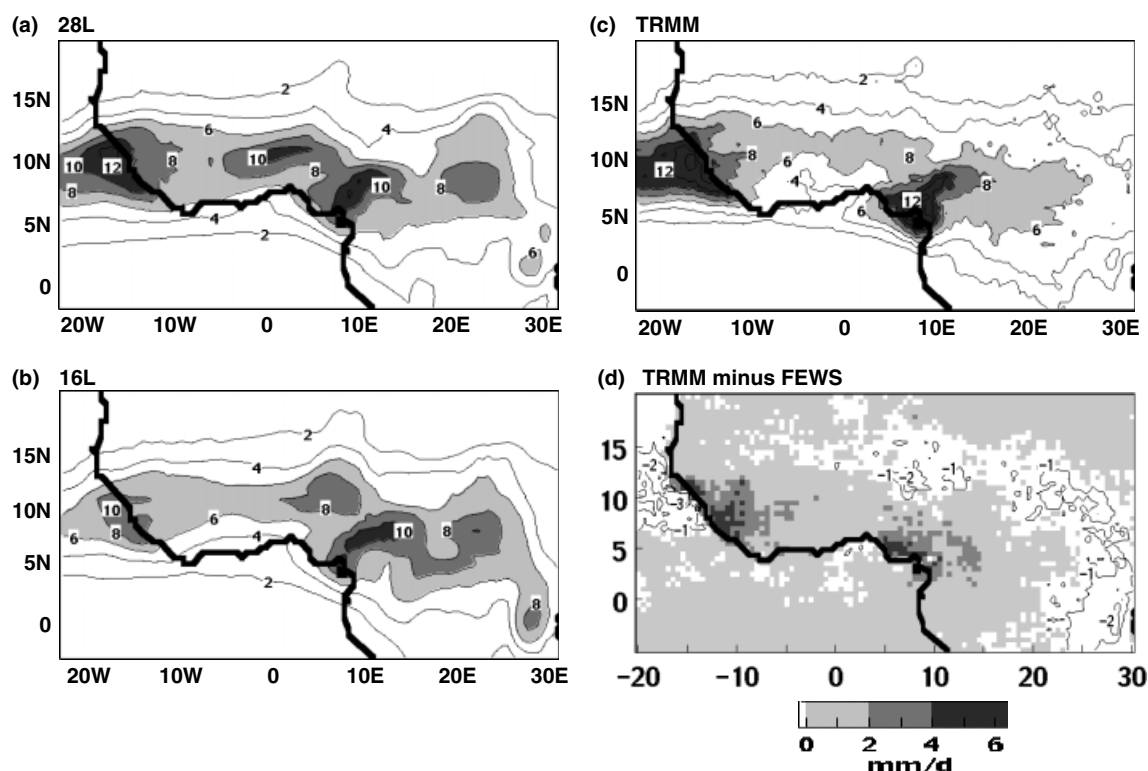

Figure 10. Spatial distributions of JJAS 1998–2003 mean rainfall rates (mm day^{-1}) for (a) RM3.28L (b) RM3.16L, (c) TRMM for 0.5° elements (courtesy DAAC/NASA GSFC), (d) TRMM minus CPC/FEWS (courtesy NOAA/CPC) for JJAS 2001–2003.

but CPC/FEWS indicates longer interruptions during July and fewer heavy rain events (>10 mm d^{-1}), especially during August and September. The higher frequency of heavy rain events by TRMM in August and September is more consistent with the RM3 results shown in Figure 11.

3.4.2. Time-longitude Hovmöller of precipitation

Westward moving precipitation areas during the summer monsoon over west Africa may be associated with squall lines or AEWs. These transient features show up as diagonal 'footprints' on Hovmöller time-longitude

distributions of the daily rainfall. The precipitation footprints usually run parallel to the swaths of alternating positive and negative *v7*, such as shown in Figure 4. Figure 13 shows the Hovmöller time-longitude distributions of the daily rainfall during JA 2003 for the 28L, 16L and TRMM. Similar distributions were prepared for the other JA periods of the study and the correlation coefficients between all pairs of distributions were computed (Table III). Note that each distribution is comprised of 5642 values (62 × 91). The correlation coefficient between the 28L results shown in Figure 13 and
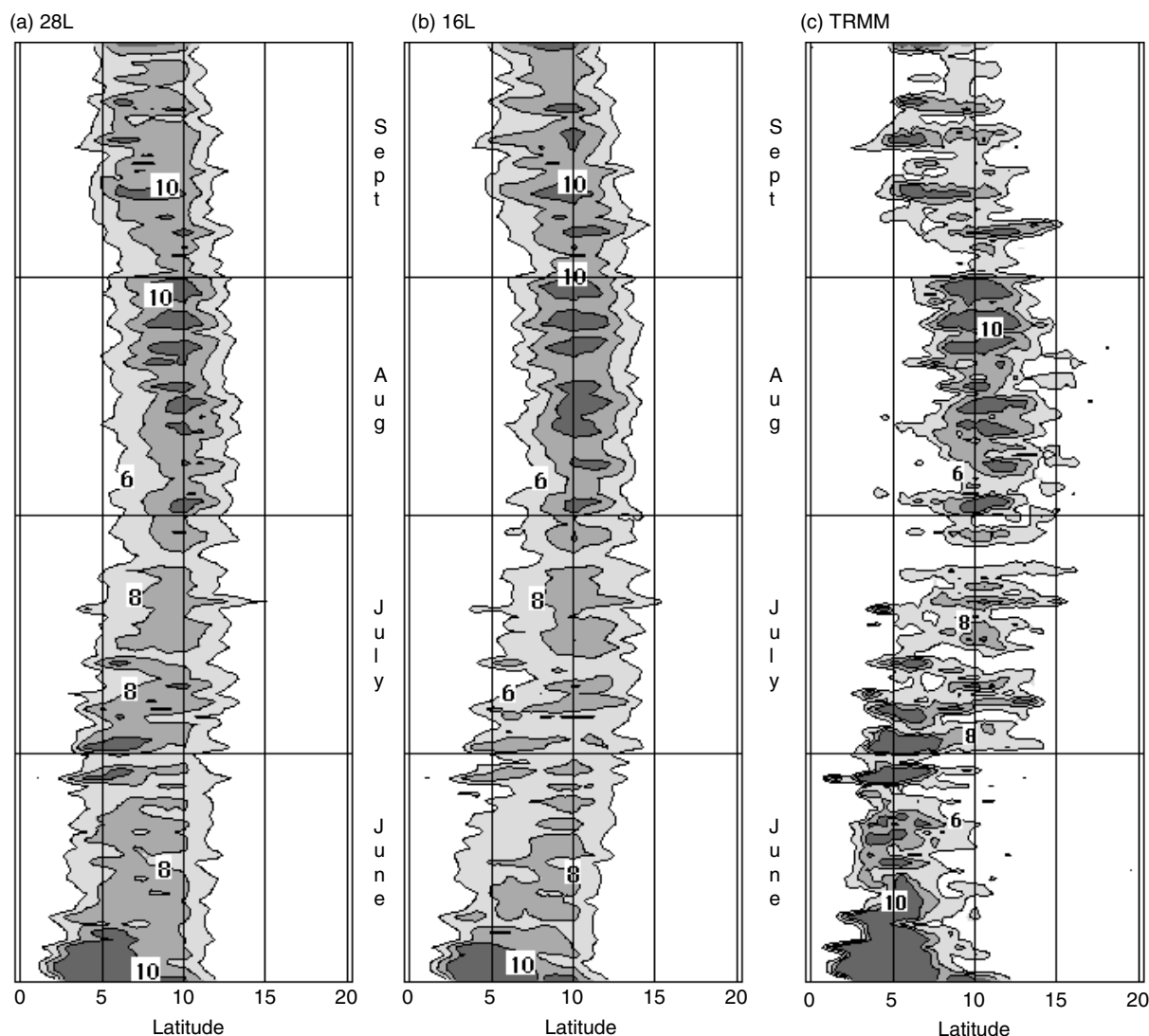
Figure 11. Hovmöller time–latitude distributions of 1998–2003 mean daily rainfall (mm), averaged between 15 °W–10 °E at each latitude, from 1 June to 30 September. (a) RM3.28L, (b) Rm3.16L, (c) TRMM for 0.5° elements (courtesy DAAC/NASA GSFC).

TRMM was 0.73 and between the 16L and TRMM, 0.74. Table III shows that the modelled precipitation rates are consistently very well correlated in time and space to the corresponding TRMM data, while the higher vertical resolution is responsible for improvements of up to 0.04 in the correlations. Note that the correlation coefficients are somewhat lower (although still statistically significant) for JA 2002 and 2003. This implies limitations in either the TRMM data for those seasons or in the NCPR data used to drive the RM3. The RM3 distributions in Figure 12 capture the diagonal swaths of heavier precipitation depicted by TRMM, but several TRMM maxima are damped.

Figure 14 shows probability density distributions of the data plotted in each of the three panels of Figure 13. While almost 30% of the TRMM values are below 2 mm day^{-1}, the threshold for the lowest 30% of RM3 results is closer to 5 mm day^{-1}. The 28L generates slightly fewer very low values than the 16L. In addition, some 5% of TRMM values exceed 19 mm day^{-1}, while the

threshold for the highest 5% of RM3 values is only about 12 mm day^{-1}. Vertical model resolution made little difference in the distribution of these daily precipitation rates, especially for the highest 50%.

Figure 15 shows time–longitude Hovmöller distributions of the 925 mb circulation divergence for JJAS 2003. Figure 15(a) and (b) gives results for the 28L and 16L, respectively. Bands of westward-propagating convergence are evident throughout the summer, although they are most distinct in mid-June and during August and September. From mid-June to early August convergence is quite weak between approximately 0–10 °E. Druyan *et al.* (2006) showed that such lower tropospheric convergence bands only partially coincide with westward-propagating precipitation swaths associated with squall lines and AEWs. Figure 15(c) shows the time-longitude Hovmöller distribution of 28L simulated August 2003 precipitation superimposed on the corresponding 925 mb divergence. Some areas of heavy rainfall do indeed coincide with strong convergence bands. However, some
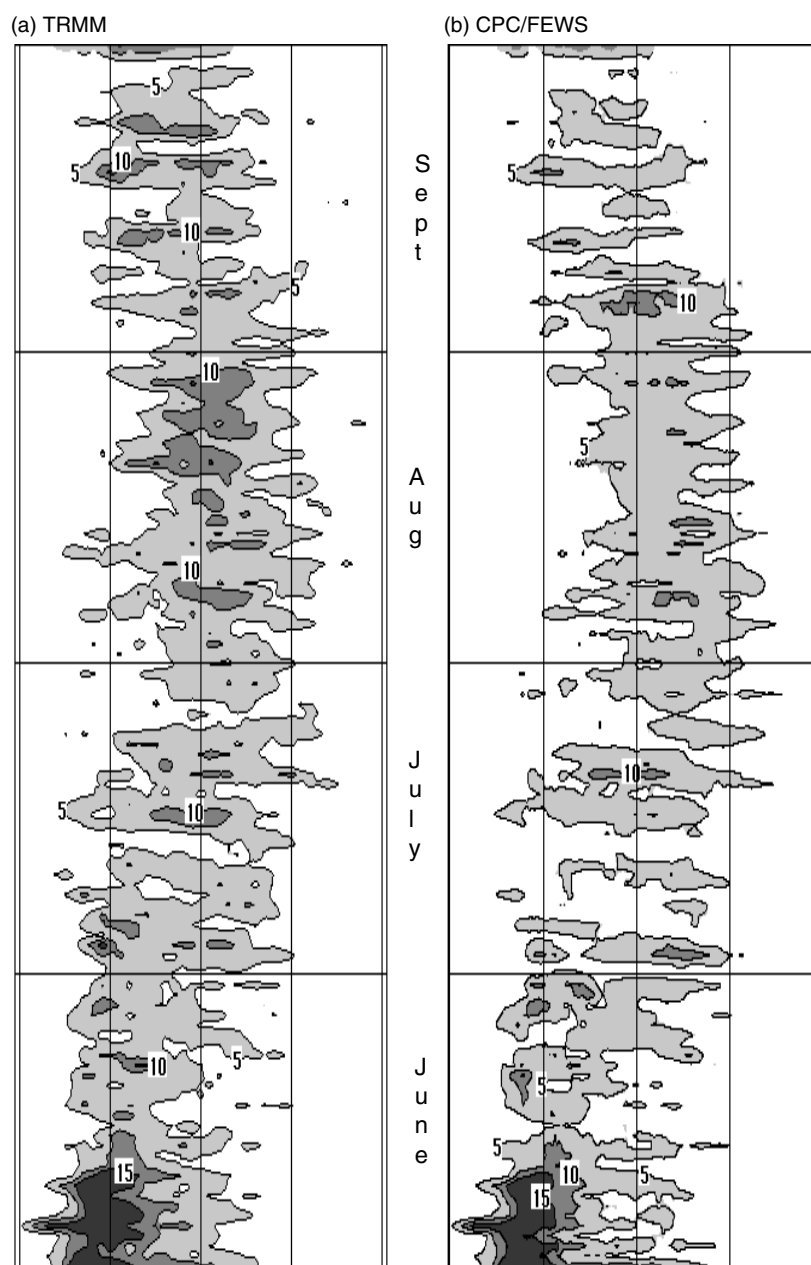
Figure 12. Hovmöller time–latitude distributions of 2001–2003 mean daily rainfall (mm), averaged between 15 °W–10 °E at each latitude, from 1 June to 30 September. (a) TRMM for 0.5° elements (courtesy DAAC/NASA GSFC), (b) FEWS/CPC for 0.1° elements (courtesy of NOAA/CPC).

westward-propagating precipitation maxima can be found outside the areas of strong convergence zones. Note that convective cells initiated by local surface heating are not always related to large-scale convergence. On the other hand, there are several relatively dry areas with convergence, presumably related to low ambient moisture or only shallow convection. Comparison of Figure 15(a) and (b) shows parallel patterns for the 28L *versus* the 16L results, but owing to the generally stronger 28L circulation, 28L convergence occupies larger time-space areas on the Hovmöller distribution. This is consistent with the probability density curves shown in Figure 14 for July–August 2003 daily precipitation, which indicate slightly higher precipitation rates for 28L than 16L over

the entire range of values. For example, while 95% of 28L values exceed 3 mm d^{-1}, only 80% of 16L values are above this threshold.

3.5. AEW composite

The structure of corresponding composite AEWs in the RM3.28L and RM3.16L simulations was studied. Seven very similar simulated AEW events from four different seasons were identified. Each was characterized by a rather high amplitude north-south trough approximately oriented along 10 °W. The events were: 9 August and 9 September, 1999, both at 06 UT; 21 August at 06 UT and 20 September at 12 UT, both 2001; 3 August at 06 UT and 7 August at 12 UT, both 2002; 10 August 2003
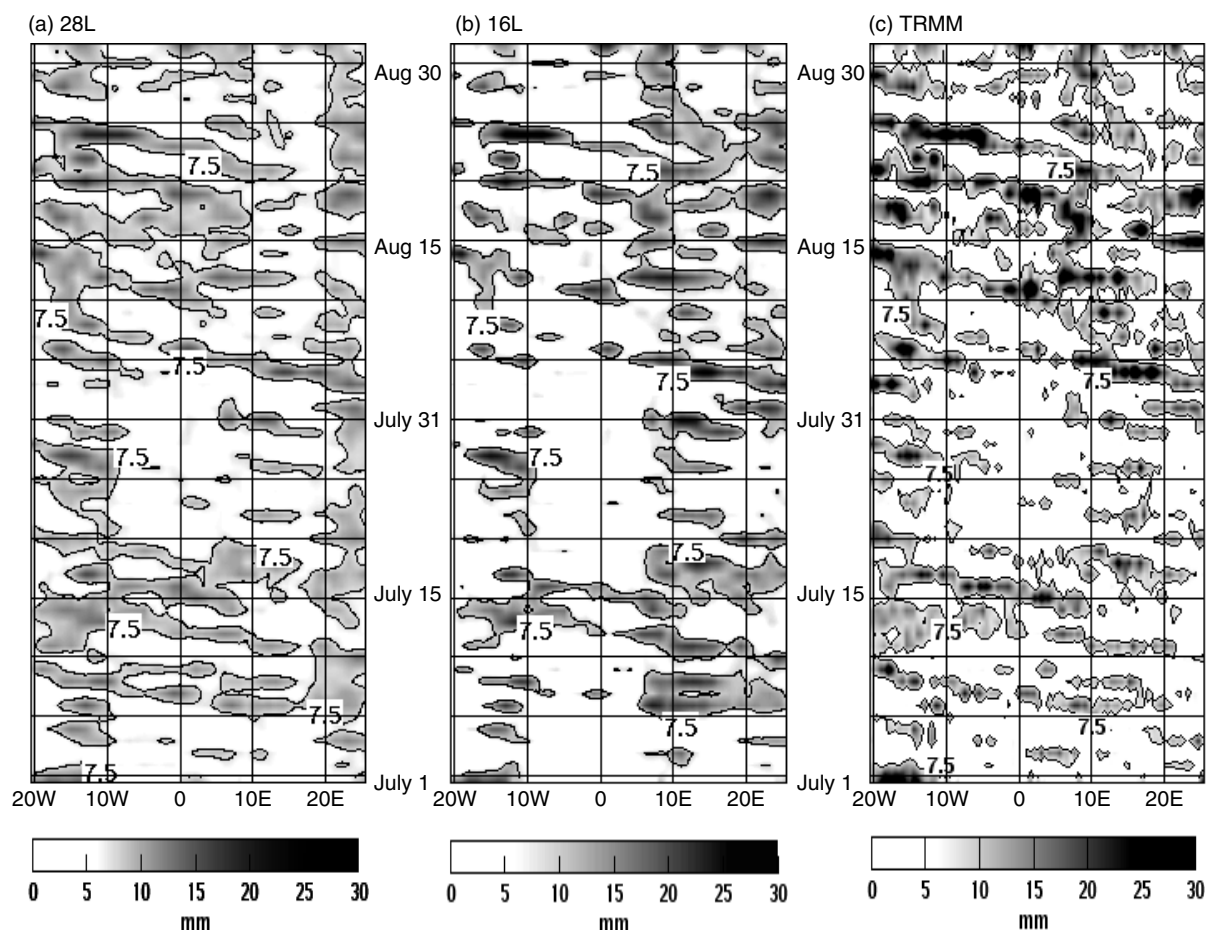
(a) 28L (b) 16L (c) TRMM

Figure 13. Hovmöller time–longitude distributions of daily rainfall (mm), averaged between 5–15 °N at each longitude for July–August 2003. (a) RM3.28L, (b) RM3.16L, (c) TRMM for 0.5° elements (TRMM data courtesy DAAC/NASA GSFC).

Table III. Correlation coefficients, means and standard deviations for time–longitude distributions the daily rainfall, such as shown in Figure 13, but for each JJAS season.

Season	cc, 28L *vs.* TRMM	cc, 16L *vs.* TRMM	cc, 28L *vs.* 16L	28L mean	16L mean	σ 28L	σ 16L	TRMM mean	σ TRMM
1998	0.94	0.91	0.92	7.0	6.7	3.9	4.0	7.1	7.9
1999	0.94	0.91	0.93	7.3	7.1	4.1	4.2	7.9	8.1
2000	0.92	0.91	0.94	6.6	5.5	3.4	3.3	6.8	7.1
2001	0.92	0.88	0.90	6.7	6.4	3.4	3.5	6.7	7.1
2002	0.72	0.70	0.88	6.6	6.3	2.7	2.9	6.7	6.7
2003	0.74	0.73	0.88	6.9	6.1	2.8	2.9	6.7	6.4
6 year	0.86	0.84	0.91	6.9	6.4	3.4	3.5	7.0	7.2

at 00 UT. The following discussion describes the three-dimensional circulation and the precipitation associated with the composite AEW of the seven events. Characteristics shared by seven AEWs are more representative than a single case study. However, the averaging of even slight differences between the structures of composite members can moderate extremes and gradients.

The composite RM3.28L 700 mb circulation indicates a north-south AEW trough along 10 °W (Figure 16(a)). The *v7* distribution for each event closely resembles the

corresponding NCPR field (not shown), indicating that the same waves occur in the RM3 and the reanalysis. RM3.28L northerlies west of the trough and southerlies east of the trough were usually several m s^{-1} weaker than corresponding NCPR data in each case. The near-surface circulation (Figure 16(b)) features on-shore winds along a considerable extent of the southwest coast of west Africa south of the vortex. The 700 mb trough for the corresponding 16L composite (Figure 16(c)) appears to have a similar amplitude, but the trough line lags several
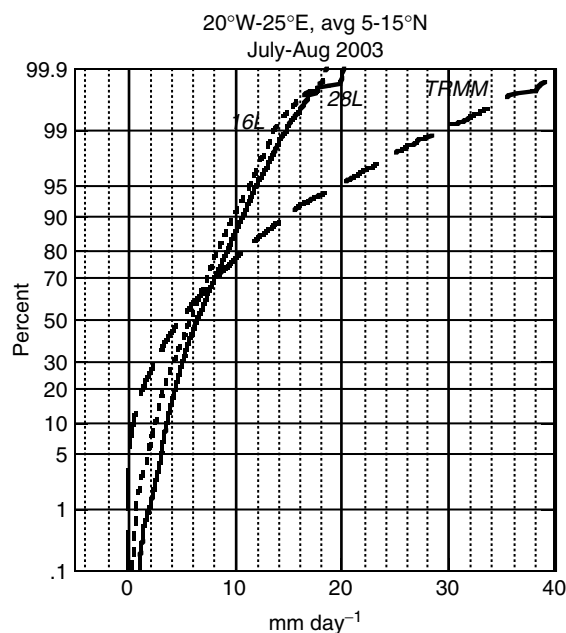
Figure 14. Pdf distributions of the data shown on the Hovmöller time–longitude distributions in Figure 13, for July–August 2003.

degrees to the east, perhaps suggesting a slower propagation speed, consistent with the weaker 16L circulation.

The 16L composite 925 mb cyclonic circulation is also displaced several degrees to the east (Figure 16(d)), so the vertical tilt is similar in both versions. The 16L near-surface cyclone is not as compact and its on-shore circulation south of the vortex is more westerly than in the 28L. Figure 17(a) shows the spatial distribution of the 28L composite vorticity of 700 mb winds. The elongated north-south maximum marks the position of the composite AEW 700 mb trough. Note the negative vorticity centres that indicate the flanking ridges to the east and west of the AEW trough. The corresponding 16L vorticity distribution (Figure 17(b)) indicates about 30% weaker vorticity extremes.

Figure 18 is a north-south cross-section of zonal wind anomalies for the 28L and 16L composites relative to August–September 1998–2003 means along 10 °W, which is close to the AEW composite trough (see Figure 16(a), (c)). Composites for the 28L and 16L versions show that the AEW strengthened the cyclonic circulation within a rather deep tropospheric layer, enhancing westerlies south of the vortex and easterlies to the north. In both cases, the centre of positive vorticity is tilted northward with altitude up to 700 mb. The centre of positive zonal wind anomalies at 600–700 mb indicates that the composite wave perturbation represents a weakening of the mean mid-tropospheric AEJ, or at least a
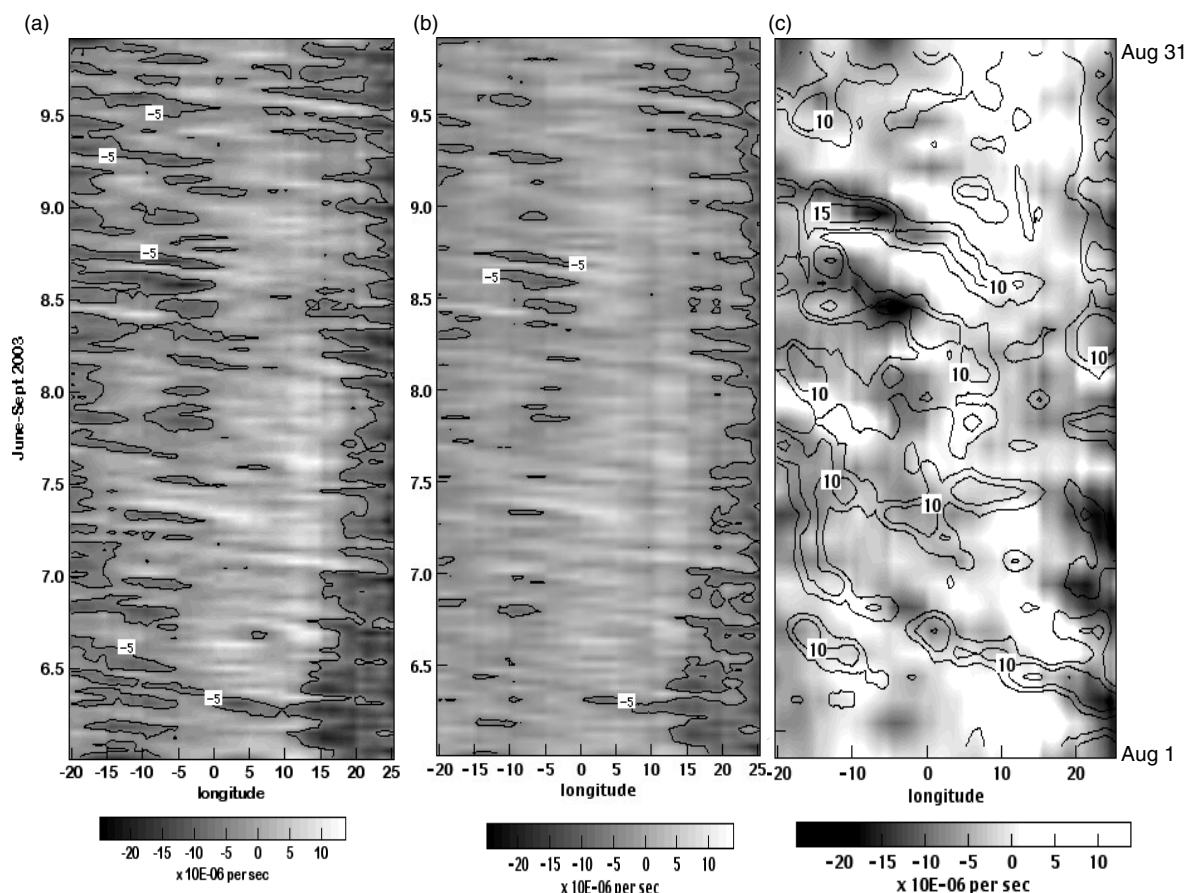

Figure 15. Hovmöller time–longitude distributions of 925 mb circulation divergence at 12 UT each day, averaged between 5–15 °N. The -5×10^{-6} s^{-1} contour is shown. (a) 28L simulation for June–September 2003 (b) 16L simulation for June–September 2003 (c) 28L simulation for August 2003 with superimposed daily rainfall (mm). Rainfall contours are 7.5, 10 and 15 mm.
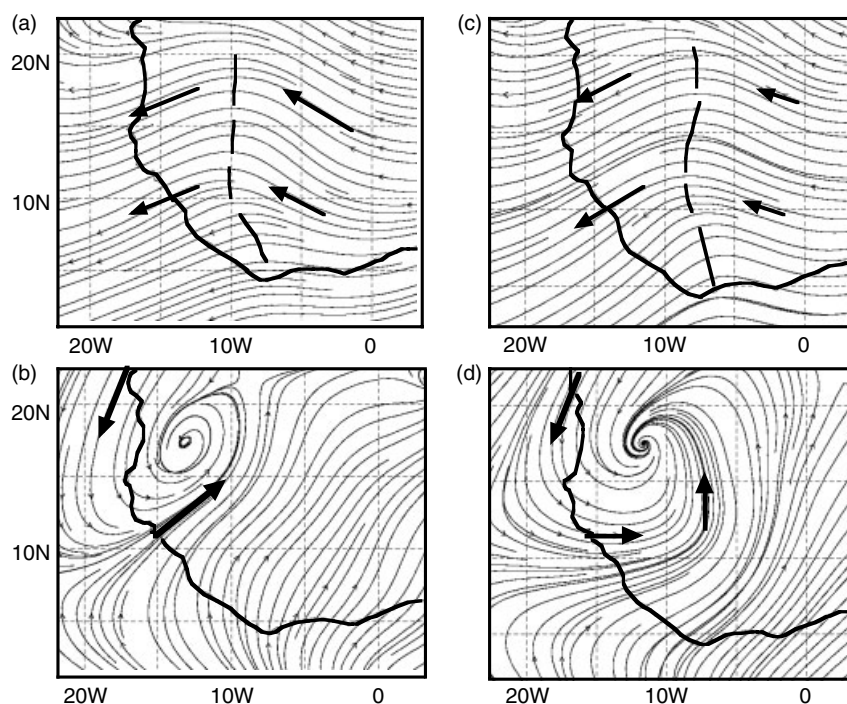
Figure 16. Composite of streamlines from u and v wind components at two vertical levels, averaged for the seven events of the composite (see text). (a) RM3.28L 700 mb, (b) RM3.28L 925 mb, (c) RM3.16L 700 mb, (d) RM3.16L 925 mb.
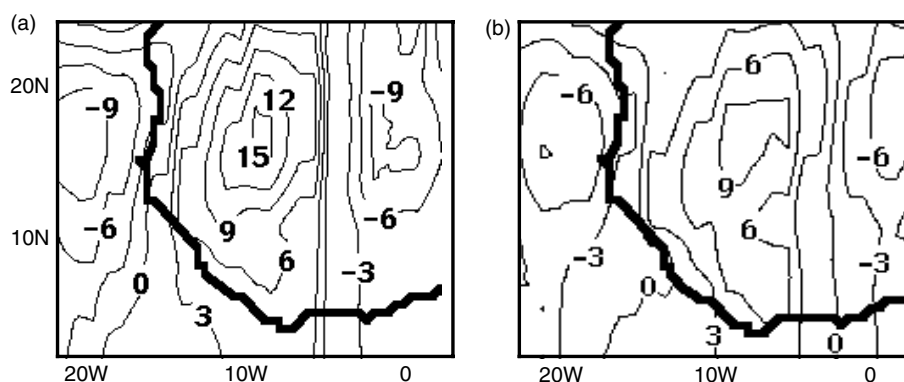

Figure 17. Vorticity of the composite 700 mb circulation from u and v wind components, averaged for the seven events of the composite. (a) RM3.28L, (b) RM3.16L. Units: $\times 10^{-6}$ s^{-1}.

northward deflection of core speeds. Accordingly, easterlies are stronger than the mean across the northern extension of the AEW near 20 °N. Westerly anomalies in the 28L composite are about 35% stronger than for 16L in the lower troposphere, although they weaken rapidly above 400 mb. The weaker 16L composite westerly anomalies peak near 400 mb, and imply a deeper cyclonic circulation.

Figure 19 shows the east–west cross-section of meridional wind (v) anomalies relative to August–September 1998–2003 means along 15 °N where the cyclonic circulation is quite strong up to about 500 mb. Enhanced northerlies are evident near 15 °W (up to 35% stronger for 28L) and enhanced southerlies near 3 °W (up to 25% stronger for 28L). Note that the zero anomaly isopleth, which is a good proxy for the trough axis, tilts eastward with altitude. Taken together, Figures 18 and 19 indicate

that the composite AEW tilts towards the northeast with altitude in the lower troposphere. The basic structure of composite wind anomalies is the same for the 28L and 16L, but vertical and horizontal wind shears are stronger for the 28L. For example over 15 °N, the 28L vertical shear of the v anomaly between 1000 and 600 mb, is -6 m s^{-1} compared to -4 m s^{-1} for 16L. The horizontal shear of the v anomaly across the vortex at 900 mb between 15 and 7 °W is about 8.5 m s^{-1} for 28L, but only about 5 m s^{-1} for 16L. The largest impact of increased vertical resolution is the more than doubling of the southerly wind anomalies at 900 mb east of the AEW vortex, with slightly weaker impacts throughout the remainder of the troposphere. The higher vertical resolution has made the vorticity especially strong within the near-surface layers, which can be deduced from the horizontal wind shears depicted in Figures 18 and 19.
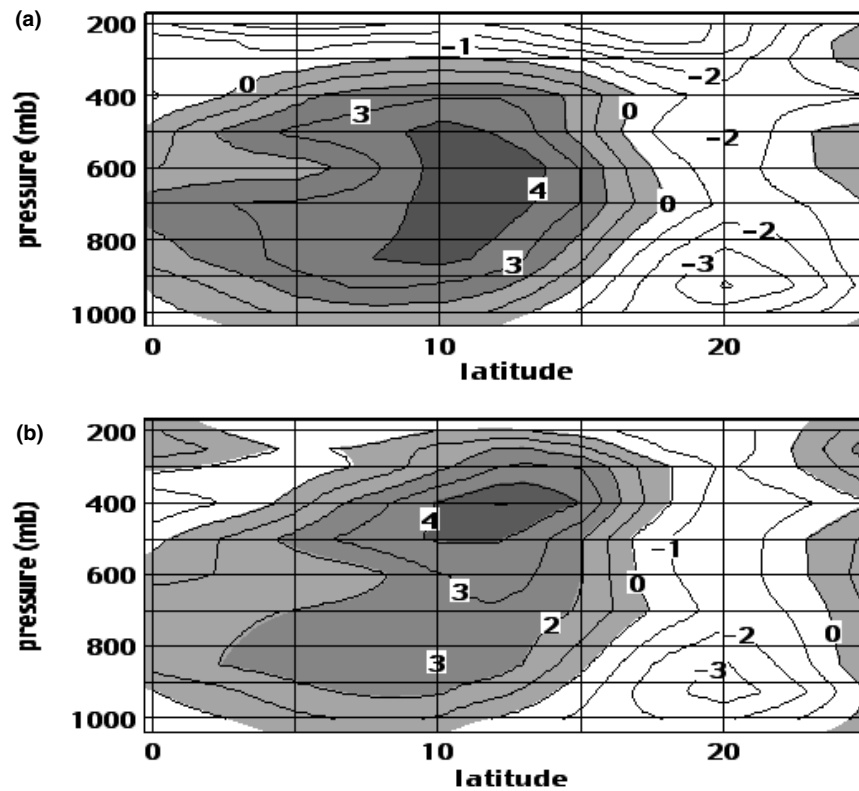
Figure 18. Zonal wind anomalies (m s^{-1}), relative to August–September 1998–2003 means, along 10°W, averaged for the seven events of the composite. (a) RM3.28L, (b) RM3.16L.
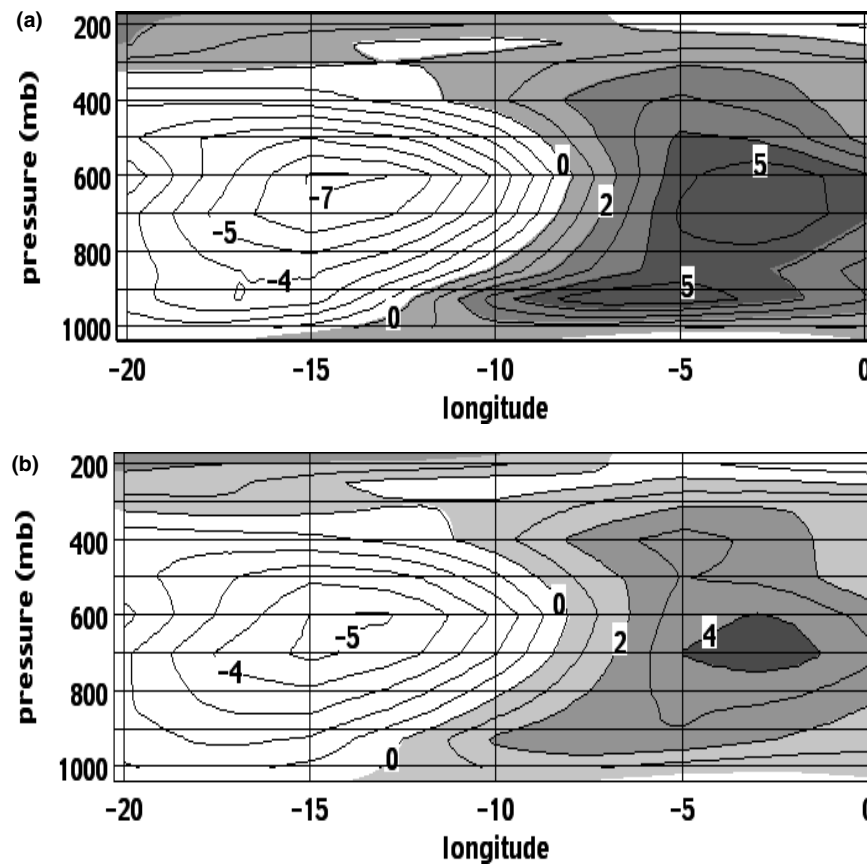

Figure 19. Meridional wind anomalies (m s^{-1}), relative to August–September 1998–2003 means, along 15°N, averaged for the seven events of the composite. (a) RM3.28L, (b) RM3.16L.

A composite precipitation distribution was constructed as the average of the 28L daily rates on each of the composite's seven calendar dates. Composite precipitation rates in Figure 20(a) are highest near 10 °N, 16 °W. The axis of maximum rainfall is along 10 °N with high rates within the Atlantic ITCZ and near the southwest coast, sections of which include orography perpendicular to the on-shore near-surface circulation (Figure 16(b)). Note in Figure 20(b) that the composite rainfall is enhanced relative to August–September means southwest of the near-surface vortex, conforming to classical models of AEW structure (Reed *et al.*, 1977). Negative precipitation anomalies occur eastward from the 700 mb trough and west of the system near the entrance to the next ridge. Figure 20(c) indicates an almost identical precipitation anomaly pattern for the 16L composite. In fact, 16L composite precipitation rates (not shown) were systematically lower than 28L composite rates, but 16L seasonal mean rates were similarly lower (as for example in Figure 10). One of the events of the composite, on 10 August 2003, can be seen in broader context by reference to Figure 13. It is evident that the event's rainfall near 15 °W was the consequence of a westward-propagating precipitation band originating near 25 °E on 3 August.

Figure 21(b) shows the 925 mb divergence field for the 28L composite. Strong lower tropospheric convergence occurs on the north side of the cyclonic vortex where the humidity is too low to support precipitation. This area is also just west of the 700 mb trough (Figure 16(a)). The second area of strong convergence is southwest of the near-surface vortex, overlapping the area of heavy precipitation rates (Figure 20(a)). The cyclonic centre and the rest of the rain belt coincide with weaker convergence. The anomalous rainfall attributable to the AEW along the Atlantic coast occurs within an area of positive vorticity advection at 700 mb, and strong 925 mb convergence. While the 28L and the 16L versions of the 200 mb composite divergence field (Figure 21(a) and (c), respectively) are quite similar, higher vertical resolution has more of an impact on the near-surface divergence (compare Figure 21(b) to Figure 21(d)). Instead of values more extreme than -10×10^{-6} s^{-1} along the coast from the rather sharp ITCZ confluence produced by the 28L, the 16L has generated rather broad westerlies near 10 °N with a more diffuse confluence and hence divergence less extreme than -10×10^{-6} s^{-1}. These differences in the convergence have had no impact on the composite precipitation anomalies (Figure 20) because both the composite and mean precipitation rates are some 15% higher for the 28L.

Upper tropospheric divergence can be either the consequence of spatially broad areas of moist convection, or the impetus for the positive vertical motion that promotes convective rainfall. Figure 21(a) and (c) show that an area of 200 mb divergence for the composite is situated between anti-cyclonic circulation turning to the north and circulation turning towards the Equator on the south side. The heaviest composite precipitation (Figure 20(a)) coincides with this band of divergence aloft, although no
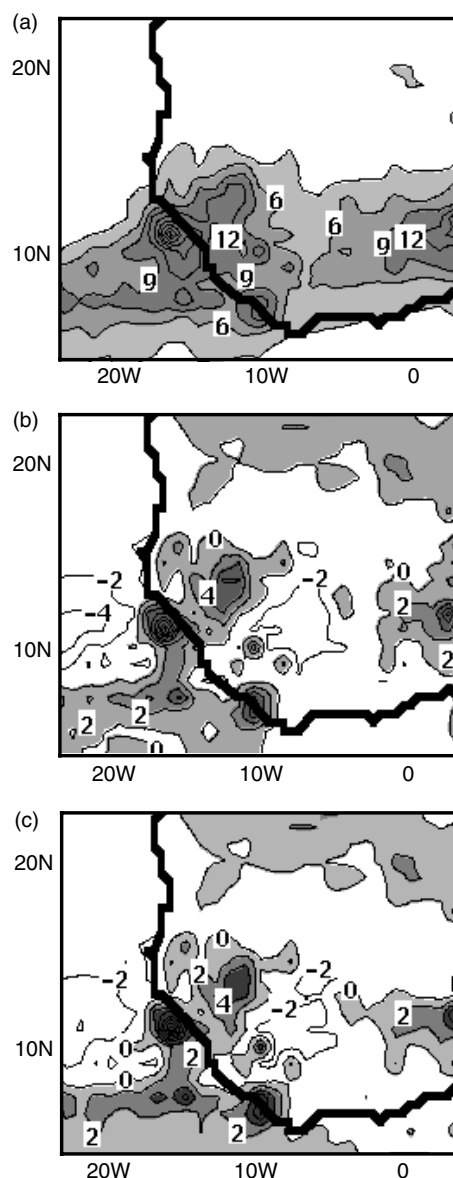

Figure 20. (a) RM3.28L precipitation rates, averaged for the seven events of the composite, (b) RM3.28L anomalies of the composite, (c) RM3.16L anomalies of the composite. Anomalies relative to August–September, 1998–2003 means. Units: mm day^{-1}.

localized divergence maxima are evident corresponding to specific precipitation centres.

3.6. Cumulus convection

The 28 and 16L simulations for JJAS 2003 were rerun with additional diagnostics that monitor the characteristics of moist convection. The moist convection scheme computes one set of diagnostics for shallow convection and a second set for deep convection. Shallow convection is defined to occur whenever the rising plume does not penetrate the 700 mb level. In deep convection, the plume rises at least 450 mb between the cloud base and top. The diagnostics compute the heating rates from condensation within the rising convective plumes for each of the two categories, shallow and deep convection. In
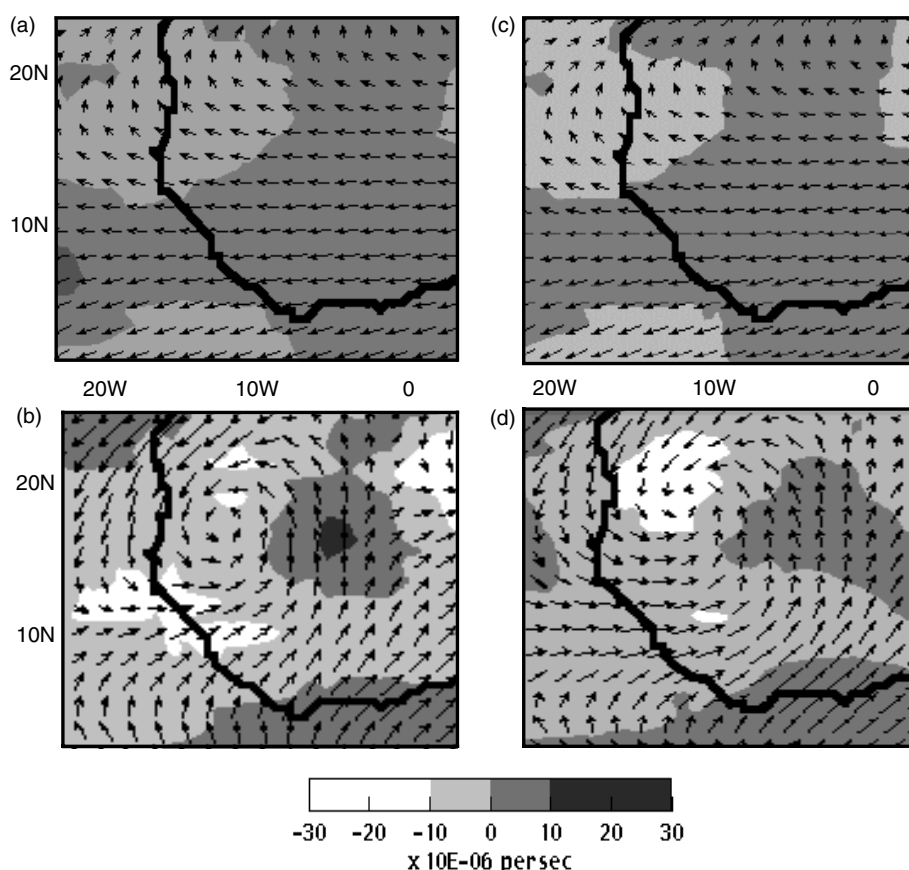
Figure 21. Divergence of u and v averaged for the seven events of the composite and superimposed over the corresponding composite circulations: (a) RM3.28L at 200 mb, (b) RM3.28L at 925 mb, (c) RM3.16L at 200 mb, (d) RM3.16L at 925 mb. Units: $\times 10^{-6}$ s^{-1}.

addition, the relative frequency of shallow *versus* deep convection is also monitored.

Figure 22 shows the vertical profiles of heating rates averaged over the ITCZ rain band, 5–10 °N, 15 °W–10 °E, for June 2003, August 2003 and for the entire JJAS season. Individual monthly peaks are between 3 and 4 K day^{-1}, but their levels vary from month to month. RM3.28L cumulus heating rate peaks are all greater than corresponding RM3.16L peaks by 10–40%. There are small differences in the levels of peak heating owing to the vertical resolution, but no generalization is suggested by the results. The higher 28L peaks are consistent with greater 28L rainfall rates, as discussed in Section 3.3.

Table IV shows the frequencies of shallow and deep convection over the same area for each month and for JJAS 2003. Except for June, the simulations at higher vertical resolution experienced higher frequencies of deep convection, although only by 2–6%. This small difference cannot account for the higher 28L peaks of cumulus heating rates.

4. Discussion and conclusion

RM3 climate simulations of six west African summer monsoon seasons were performed at two vertical resolutions of the model, but at the same horizontal

Table IV. Monthly and seasonal mean frequencies of moist shallow and deep convection simulated by the RM3.28L and RM3.16L during June–September 2003, averaged over 5–15 °N, 15 °W–10 °E.

	RM3.28L		RM3.16L	
	Shallow	Deep	Shallow	Deep
June	43	55	43	57
July	38	70	45	64
August	44	76	42	74
September	18	68	17	64
June–Sept	36	67	37	65

resolution of 0.5° grid spacing. A previous study (Druyan *et al.*, 2006) documented the performance of the 16L version and here simulations for the same seasons were repeated with the 28L version. All simulations were initialized with NCPR atmospheric conditions, sea-surface temperatures (SST) and soil moisture on 15 May and driven by NCPR SST and NCPR synchronous atmospheric lateral boundary conditions taken four times per day throughout each JJAS season. The main difference in the results was that the 28L produced stronger circulation within the near-surface monsoon flow and at the level of the mid-tropospheric AEJ. Additional vertical levels of
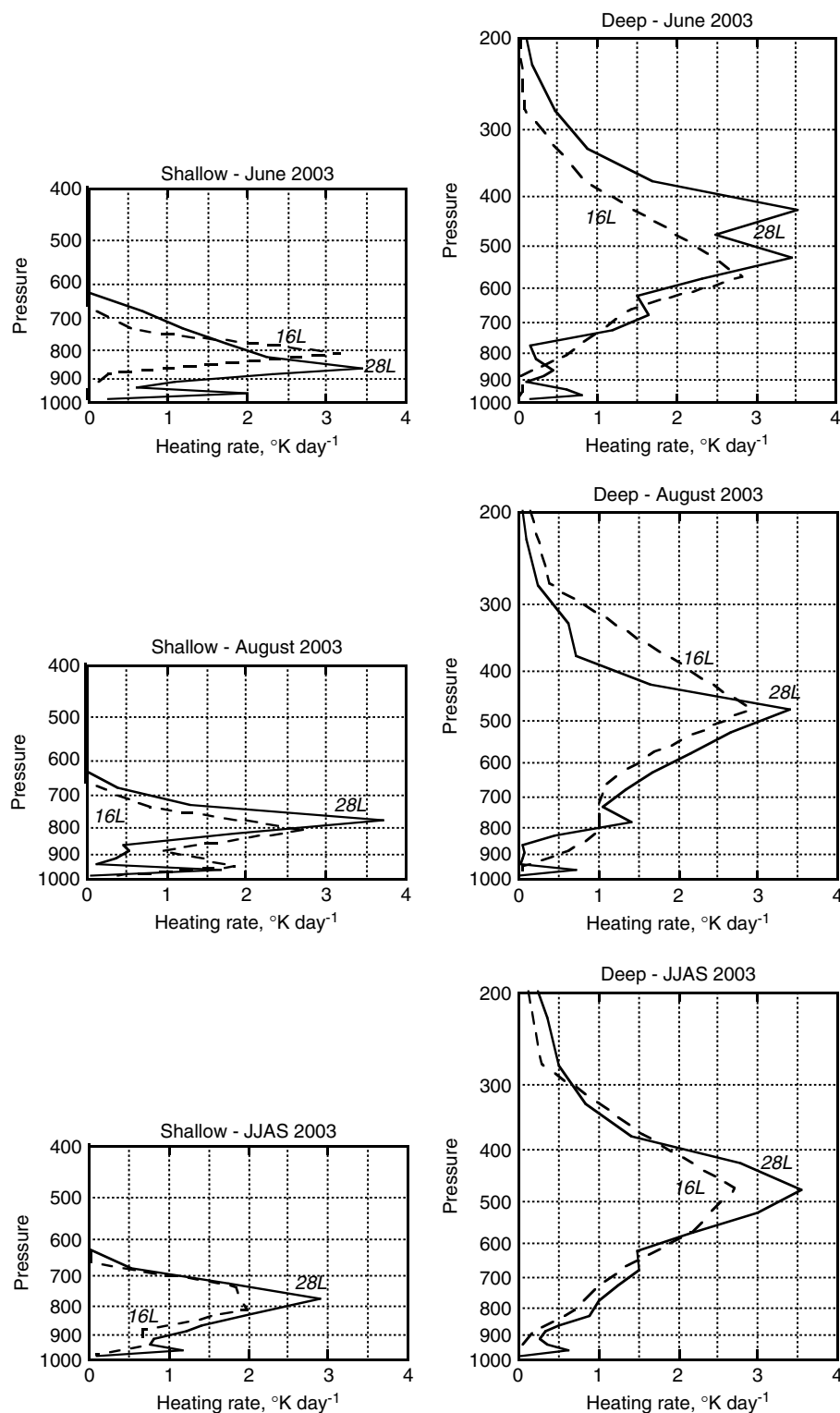
Figure 22. Profiles of cumulus heating rates from shallow and deep moist convection for RM3.16L and RM3.28L for June, August and June–September, 2003, averaged over 5–10 °N, 15 °W–10 °E.

the 28L allowed greater negative zonal wind shear, resulting in a six-season JJAS mean AEJ core speed for the 28L that was about 4 m s^{-1} faster than the corresponding 16L and NCPR data. Stronger near-surface monsoon westerlies and Harmattan easterlies of the 28L match NCPR, while the 16L near-surface circulation is about 1 m s^{-1} weaker.

Spatial patterns of both 700 mb vorticity variance and spectral amplitudes of 700 mb meridional wind ($v7$) time series for 3–6 day periodicities were almost identical at the two model resolutions, but the stronger 28L 700 mb circulation produced 50% higher vorticity variances and 20% higher spectral amplitudes, both of which are indicators of AEW tracks.

Time series of *v7* averaged over $5-15\,°$N for the RM3 at both resolutions were almost perfectly correlated with corresponding NCPR time series. Druyan *et al.* (2006) showed that RM3.16L oscillations of *v7* caused by transient AEWs were often only a fraction of corresponding NCPR *v7* variability. Results here demonstrate that increasing the model's vertical resolution to 28L increases the amplitudes of simulated AEWs. Typical standard deviations of *v7* were increased from 75 to 93% of NCPR values. Evidence was presented that the high correlation between RM3 and NCPR timing and location of AEW traversals is not a consequence of the simple propagation of waves from the eastern boundary through the domain. Rather, the study showed that AEWs develop and grow in amplitude within the RM3 domain, manifest by increasingly stronger *v7* oscillations, increasingly stronger spectral amplitudes at $3-6$ day periods and increasingly larger vorticity variances that double in magnitude from east to west between $30\,°$E and $15\,°$W. The RM3 develops and propagates the waves in close synchrony with the NCPR model treatment and in agreement with observations that are assimilated by NCPR.

The 28 and 16L produce somewhat different JJAS mean precipitation fields. Using TRMM data for validation, the 28L gives the more appropriately higher Atlantic ITCZ and southwest west Africa coastal maximums, while the 16L produces more appropriately lower mean rates over the interior of west Africa. Cumulus heating rate peaks for both shallow and deep moist convection within the west Africa precipitation maximum were also consistently higher for the 28L simulations. These higher peak heating rates may be supplying some of the energy for stronger AEWs. Both versions offer a fairly realistic northward advance of the rain belt during early summer, although the 28L six-summer means matched the TRMM advance better during June. Time–longitude distributions of daily rainfall were correlated with corresponding TRMM estimates with coefficients greater than 0.90 in four out of six seasons. Higher vertical resolution of the 28L gave only slightly higher correlations, but not a higher range of values. Both versions produce too few near-zero events and too few very heavy precipitation events compared to TRMM. Although 28L featured more frequent and more spatially contiguous areas of strong near-surface convergence compared to 16L in the one season that was examined, precipitation rates were only marginally increased, and then over the entire range.

A composite AEW composed of seven RM3.28L simulated wave events was compared to the corresponding 16L composite. It featured an intense cyclonic circulation at 925 mb displaced slightly westward from a 700 mb trough. Cross-sections of zonal and meridional winds showed that cyclonic vorticity was stronger than the August–September mean from the surface up to about 400 mb, with the centre of circulation tilted towards the northeast with altitude. The 28L version featured higher vorticity anomalies and higher vorticity at 700 mb. Composite rainfall was anomalously high southwest of the cyclone vortex and anomalously low east of

the 700 mb trough. The composite precipitation anomaly pattern was identical for the 28 and 16L versions. The area of highest anomalous rainfall corresponded to a centre of extreme low-level convergence in the 28L case only. The rainiest areas, however, did generally overlap 925 mb convergence and 200 mb divergence. The AEW was shown in one example to be associated with a westward-propagating swath of precipitation.

This comparison in the performances of the 16 and 28L versions was made by increasing the vertical resolution of the 16L, with no other adjustments to the model code. Optimization trials are underway to improve the simulated 28L precipitation distributions by adjusting coefficients that determine the strength of horizontal moisture convergence, by adjusting the steepness of topographic relief and by decreasing internal horizontal smoothing of variables.

Acknowledgements

References

Burpee R. 1972. The origin and structure of easterly waves in the lower troposphere of North Africa. *Journal of the Atmospheric Sciences* **29**: 77–90.

Del Genio A, Yao M-S. 1993. Efficient cumulus parameterization for long-term climate studies. The GISS scheme, in *Cumulus Parameterization*, vol. 24, Emanuel K, Raymond D (eds). American Meteorological Society Monograph Series: Boston; 181–184.

Del Genio A, Yao M-S, Kovari W, Lo K-W. 1996. A prognostic cloud water parameterization for global climate models. *Journal of Climate* **9**: 270–304.

Diedhiou A, Janicot S, Viltard A, de Felice P, Laurent H. 1999. Easterly wave regimes and associated convection over West Africa and tropical Atlantic: results from NCEP/NCAR and ECMWF reanalyses. *Climate Dynamics* **15**: 795–822.

Druyan L, Fulakeza M. 2005. Mesoscale climate analysis over West Africa. *CLIVAR Exchanges* **10**(20): 34–35.

Druyan L, Lonergan P, Saloum M. 1996. African wave disturbances and precipitation at Niamey during July-August. 1987 and 1988. *Climate Research* **7**: 71–83.

Druyan L, Fulakeza M, Thiaw W. 2000. Regional model simulations of African wave disturbances. *Journal of Geophysical Research* **105**: 7231–7255.

Druyan L, Fulakeza M, Lonergan P. 2004. Land surface influences on the West African summer monsoon: implications for synoptic disturbances. *Meteorology and Atmospheric Physics* **86**: 261–273.

Druyan L, Fulakeza M, Lonergan P. 2006. Mesoscale analyses of West African summer climate: focus on wave disturbances. *Climate Dynamics* **27**: 459–481.

Druyan L, Fulakeza M, Lonergan P, Saloum M. 2001. A regional model study of synoptic features over West Africa. *Monthly Weather Review* **129**: 1564–1577.

Duvel JP. 1990. Convection over tropical Africa and the Atlantic Ocean during northern summer. Part II: modulation by easterly waves. *Monthly Weather Review* **118**: 1855–1868.

Fortune M. 1980. Properties of African squall lines inferred from time-lapse satellite imagery. *Monthly Weather Review* **108**: 153–168.

Fritsch M, Carbone R. 2004. Improving quantitative precipitation forecasts in the warm season. *Bulletin of the American Meteorological Society* **85**: 955–965.

Hansen J, Sato MKI, Nazarenko L, Ruedy R, Lacis A, Koch D, Tegen I, Hall T, Shindell D, Santer B, Stone P, Novakov T, Thomason L, Wang R, Wang Y, Jacob D, Hollandsworth S, Bishop L, Logan J, Thompson A, Stolarski R, Lean J, Willson R, Levitus S, Antonov J, Rayner N, Parker D, Christy J. 2002. Climate forcings in Goddard institute for space studies SI2000 simulations. *Journal of Geophysical Research* **107**: 4347, DOI: 10.1029/200IJD001143.

Herman A, Kumar V, Arkin P, Kousky J. 1997. Objectively determined 10-day African rainfall estimates created for famine early warning systems. *International Journal of Remote Sensing* **18**: 2147–2159.

Inness P, Slingo J, Woolnough S, Neale R, Pope V. 2001. Organization of tropical convection in a GCM with varying vertical resolution; implications for the simulation of the Madden-Julian oscillation. *Climate Dynamics* **17**: 777–793.

Lamb P, Peppler R. 1991. West Africa. In *Teleconnections: Linkages Between ENSO, Worldwide Climate Anomalies, and Societal Impacts*, Glantz MH, Katz RW, Nicholls N (eds). Cambridge University Press; Cambridge, UK: 121–189.

Landsea C, Gray W. 1992. The strong association between western Sahelian monsoon rainfall and intense Atlantic hurricanes. *Journal of Climate* **5**: 435–453.

Lavaysse C, Diedhiou A, Laurent H, Lebel T. 2006. African easterly waves and convective activity in wet and dry sequences of the West African monsoon. *Climate Dynamics* **27**: 319–332.

Leung L, Qian Y, Bian X, Washington W, Han J, Roads J. 2004. Mid-century ensemble regional climate change scenarios for the western US. *Climatic Change* **62**: 75–113.

New M, Lister D, Hulme M, Makin I. 2002. A high-resolution data set of surface climate over global land areas. *Climate Research* **21**: 1–25.

Pytharoulis I, Thorncroft C. 1999. The low-level structure of African easterly waves in 1995. *Monthly Weather Review* **127**: 2266–2280.

Reed R, Norquist D, Recker E. 1977. The structure and properties of African wave disturbances as observed during phase III of GATE. *Monthly Weather Review* **105**: 317–333.

Reed R, Klinker E, Hollingsworth A. 1988. The structure and characteristics of African easterly wave disturbances as determined from the ECMWF operational analysis/forecast system. *Meteorology and Atmospheric Physics* **38**: 22–33.

Rosenzweig C, Abramopoulos F. 1997. Land-surface model development for the GISS GCM. *Journal of Climate* **10**: 2040–2054.

Thorncroft C, Blackburn M. 1999. Maintenance of the African easterly jet. *Quarterly Journal of the Royal Meteorological Society* **125**: 763–786.

Thorncroft C, Hodges K. 2001. African easterly wave variability and its relationship to Atlantic tropical cyclone activity. *Journal of Climate* **14**: 1166–1179.

Ward MN, Cook K, Diedhiou A, Fontaine B, Giannini A, Kamga A, Lamb PJ, Ben Mohamed A, Nassor A, Thorncroft C. 2004. Seasonal-to-decadal predictability of West Africa climate. *CLIVAR Exchanges* **9**(3): 14, 19–20.